

Stefan Fortmüller, BSc

Feasibility study of the Friction Surfacing as an alternative Additive Manufacturing technique for titanium alloys

MASTER'S THESIS

to achieve the university degree of
Diplom-Ingenieur
Master's degree programme: Advanced Materials Science

submitted to

Graz University of Technology

Supervisor

Univ.-Prof. Dr. Ing. Sergio de Traglia Amancio Filho

Co-Supervisor

Carlos Alberto Belei Feliciano Bach. Mestr.
Institute of Materials Science, Joining and Forming

Graz, September 2020

AFFIDAVIT

I declare that I have authored this thesis independently, that I have not used other than the declared sources/resources, and that I have explicitly indicated all material which has been quoted either literally or by content from the sources used. The text document uploaded to TUGRAZonline is identical to the present master's thesis.

Date, Signature

Contents

1	Abstract	6
2	Kurzfassung	7
3	Introduction	8
3.1	Basics of the friction surfacing process	8
3.1.1	State of the art for single-layer friction surfacing	9
3.1.2	Ti-64 in friction surfacing	10
3.1.3	Friction surfacing as an additive manufacturing technique	10
3.2	Characteristics of titanium alloys	13
3.2.1	α - β -alloys	13
3.2.2	Martensite formation in titanium	14
4	Materials and Methods	15
4.1	Materials	15
4.2	Experimental methods	15
4.2.1	Friction stir welding machine	15
4.2.2	Choice of parameters and deposition evaluation	16
4.2.3	Temperature measurements	18
4.2.4	Hardness tests	18
4.2.5	Metallographic preparation	19
4.2.6	Microstructure characterization	19
5	Results and discussion	20
5.1	Deposition with an 8 mm rod	20
5.1.1	Microstructural characterization of the 8 mm rod layer	23
5.1.2	Hardness tests of the 8 mm depositions	25
5.2	Depositions with a 12 mm rod	26
5.2.1	Influence of force on the layer appearance	28
5.2.2	Temperature measurements	31
5.2.3	Hardness tests of the 12 mm rod depositions	32
5.2.4	Influence of rod diameter on the layer formation	33
5.3	Double-layer deposition with a 12 mm rod	35
5.3.1	Microstructural characterization of the double-layer	36
5.3.2	Hardness tests of the double-layer	37
6	Summary and Outlook	40
	References	41

1 Abstract

In recent years the interest in additive manufacturing has increased drastically, due to its benefit of constructing metal parts of near net shape and the possibility of generating unique shapes for custom applications. The most used additive manufacturing technologies, like powder bed fusion or wire arc additive manufacturing, are all fusion based processes, meaning that the melting temperature of the metal is reached during the layer by layer production. Even though these processes are well established and investigated, a few problems arise, for instance shrinkage defects and porosity caused by reaching the melting temperature, which subsequently leads to the degradation of the mechanical properties. Because of this, a friction based solid-state additive manufacturing method is in high demand, where the melting temperature is not reached and the metal is deposited by generating a viscoplastic layer, which also enables the joining of dissimilar materials. One process that fulfills these requirements is the Friction Surfacing, which uses a rotating metallic consumable rod to generate heat by friction and plasticizes the materials without melting. Since this a relatively new technique, not many material combinations have been investigated, in particular titanium alloys, remaining a vastly unexplored application area.

The aim of this work was to firstly deposit Ti-64 by friction surfacing with 8 and 12 mm rods and obtain information about the microstructure and mechanical properties. Ultimately, the results should be taken to determine if a double-layer deposition, which means that two single-layers are consecutively deposited and centered on top of each other, is feasible and how the microstructure changes in the second layer.

Although titanium exhibits a complex deformation behavior, especially when reaching temperatures above the $\alpha - \beta$ transformation, as well as strain rate sensitivity and flow instabilities, a homogenous deposition, where the flash generates on the rod, was achieved for both the 8 mm and 12 mm rods. However, the microstructure showed for both diameters some porosity, unbonded regions and the formation of regions rich in small grains of the α -phase. In order to evaluate the feasibility of the process as an alternative additive manufacturing technique, a double-layer deposition was generated with the 12 mm rods, by taking the best possible parameters from the previous experiments. The layer formation was not as stable as the single-layer, since the decreased contact surface demanded longer times for the shear layer formation during the shortening stage, which needs to be further optimized. As for the microstructure, the double-layer showed a grain enlargement in the second layer and some porosity in the transition zone. The hardness of both second and first layer was increased by the reduction in grain size and the formation of regions rich in small grains of the α -phase.

2 Kurzfassung

In den letzten Jahren ist die Wichtigkeit von additiven Herstellungsverfahren stark angestiegen aufgrund der Möglichkeit Metallbauteile mit niedrigem Materialverbrauch und speziellen Geometrien herzustellen. Die meistverbreitetsten Prozesse, wie zum Beispiel das Pulverbettverfahren oder die lichtbogenbasierte additive Fertigung, sind alle schmelzbasierende Methoden, was bedeutet, dass die Schmelztemperatur erreicht wird. Obwohl diese Prozesse gut erforscht und entwickelt sind, ergeben sich Nachteile, wie zum Beispiel Porosität oder Schrumpfungsdefekte, welche die mechanischen Eigenschaften verschlechtern. Das Reibauftragungsschweißen umgeht diese Probleme, da die Schmelztemperatur nicht erreicht wird und die Schichten mittels einer viskoplastischen Zone aufgetragen werden. Dieser Prozess verwendet einen rotierenden Metallstab, der mit der Erzeugung von Reibungswärme verbraucht und aufgetragen wird. Da das eine relativ neue Methode ist, wurden erst wenige Materialkombinationen untersucht und besonders der Bereich der Titanlegierungen ist weitestgehend unerforscht.

Das Ziel dieser Arbeit war Ti-64 mittels Reibauftragungsschweißens aufzutragen mit Stäben von 8 und 12 mm Durchmesser. Mit den Resultaten der Einzelschichten soll weiters untersucht werden ob es machbar ist zwei Schichten aufeinander aufzutragen. Obwohl Titanlegierungen ein komplexes Verformungsverhalten aufweisen, besonders über dem $\alpha - \beta$ Phasenübergang, war es möglich eine homogene Schicht mittels 8 und 12 mm Stäben aufzutragen, wo die Wulstbildung am Stab erfolgt. Dennoch zeigte die Mikrostruktur für beide Durchmesser Porosität, ungebundene Zonen und die Bildung von Scherbändern, welche kleine α -Körner aufwiesen.

Um die Machbarkeit des Prozesses als additive Herstellungsmethode zu untersuchen wurde eine Doppelschicht, mithilfe der besten Parameter, ermittelt durch die Experimente für die Einzelschicht, mit den 12 mm Stäben aufgetragen. Die Doppelschicht erwies sich als weniger stabil als die Einzelschicht, da durch die verminderte Kontaktfläche weniger Reibungswärme erzeugt wird und die Verkürzungsphase am Anfang des Prozesses verlängert wird, was noch in weiterführenden Projekten untersucht werden muss. Die Mikrostruktur zeigte in der zweiten Schicht eine Vergrößerung der Körner im Vergleich zur ersten Schicht und minimale Porosität in der Übergangszone. Die Härte sowohl der ersten als auch der zweiten Schicht stieg an, verursacht durch die Reduktion der Korngröße und die Bildung von sauerstoffstabilisierten Zonen, welche aus der α -Phase bestanden.

3 Introduction

3.1 Basics of the friction surfacing process

The Friction Surfacing process is normally used for the repair of worn or damaged parts or to increase the corrosion resistance and is based on the plastic deformation of the used metal [1]. In order to plasticize the metal, frictional heat is produced by using a rotating metallic consumable rod that is pressed against a substrate, with a specific axial force, rotates with a certain rotational speed and moves in the direction of the deposition with a given traverse speed. In the first stage of the process, as it can be seen in Fig. 3.1, also called the shortening stage (b), the rotating rod is pressed against the substrate, without a traverse movement, until the quasi-liquid visco-plastic shear layer is formed (c) and a deposition is possible (d). Following that, a traverse movement of the rod is applied and a layer along the direction of the travel speed is produced [1].

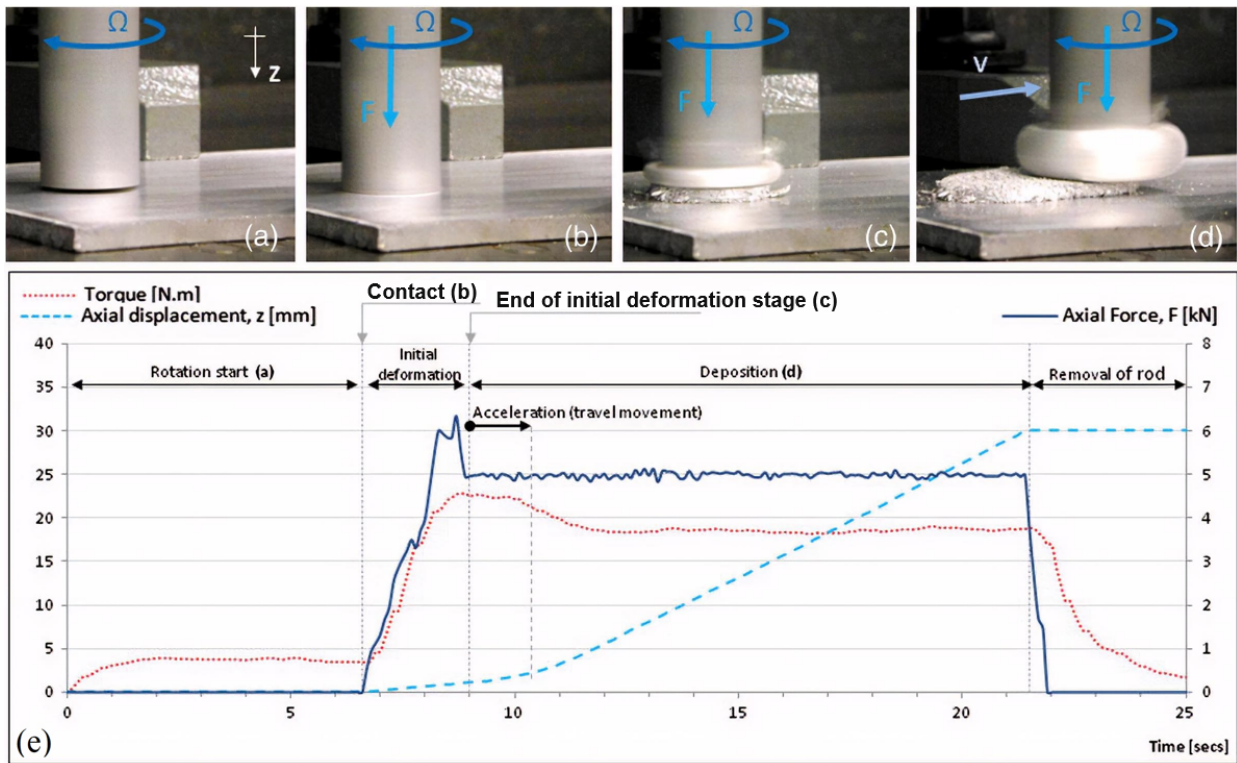


Fig. 3.1: Stages of Friction Surfacing: (a) Rod is rotating with the rotational speed Ω ; (b) Axial force \vec{F} is applied in the z -direction; (c) Shear layer is formed by frictional heat, also called the shortening stage; (d) Traverse speed v is applied to deposit the layer. Also, the torque, axial displacement and axial force curves are shown (e), where a sharp increase in force, as well as torque, is visible at the first contact between rod and substrate, followed by a constant trend during the deposition. Adapted from [2].

This layer can be formed by the existence of a viscoplastic solid-state region also called “third-body region” that still stays in the solid-state, but exhibits a flow pattern, normally characteristic for a fluid. Moreover, this zone reaches temperatures above the recrystallization point, but always stays below the melting point, being all the heat generated by friction dissipation. In Fig. 3.2 these thermomechanical regions of the process can be seen (c), as well as the origin of the mushroom shaped flash coming from the viscoplastic layer and the cross section (a) visualized with the process variables indicated on (b) [3].

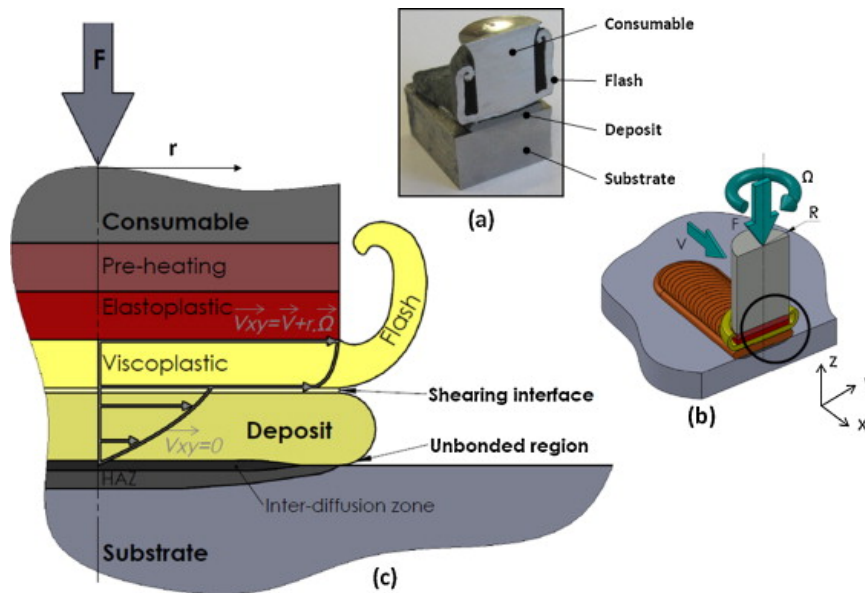


Fig. 3.2: (a) Cross section of layer with the rod; (b) Process variables; (c) Thermomechanical regions of FS, where the viscoplastic region forms between the deposition and the elastoplastic region [3].

3.1.1 State of the art for single-layer friction surfacing

Due to FS being a relatively novel manufacturing technique, only a handful of studies have been done on this topic. But nevertheless, a wide range of materials were already successfully deposited, such as steels [4], aluminium [5], magnesium [6], titanium [7] and NiAl bronze [8]. Normally diameters equal or greater than 20 mm are used, which limits the application possibilities. This was shown by Vitanov and Voutchkov [9], for stainless steels, where it was concluded that by decreasing the diameter by 50% the bonding time is also reduced by this factor, consequently leading to the usage of wider rod diameters, giving the process more time to occur and complete.

The visual appearance of a typical FS layer can be seen in Fig. 3.3 with its characteristic ripple-like features and slight offset between the center of the layer and the contact point of the rod.

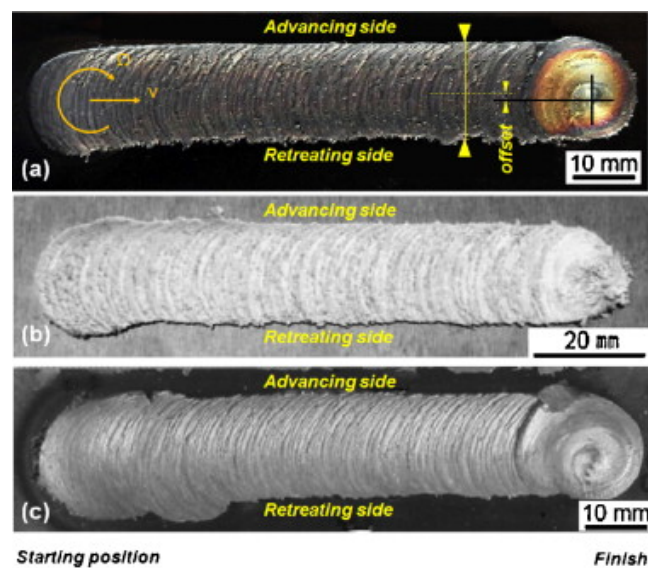


Fig. 3.3: Typical shape of FS layers for different aluminium alloys. a) AISI H13 over AISI 1020 [10]; b) AA2017 over AA5052 [11] and c) AISI 310 over AISI 1020 [12].

3.1.2 Ti-64 in friction surfacing

Due to Ti-64 being a highly complex material, caused by its deformation behavior and flow instabilities especially around the β -transus temperature [13–15], not much data is available for its application in friction surfacing. As of now, a constant and homogenous single-layer deposition of Ti-64 with a 20 mm rod was achieved by [7, 16–21] with the corresponding depositions and micrographs shown in Fig. 3.4. Fitseva [20] showed that two different rotational speed regimens are present, where at low temperatures the flash was generated at the substrate, with temperature fluctuations. At higher rotational speeds the flash formed mostly at the rod and the temperature was constant. Furthermore, the impact of rotational speed on the stability of process was studied by [7] and [18] for Ti Grade 1 and Ti-64, where the conclusion was drawn that a higher rotational speed leads to a more homogenous, thicker and wider deposition. As stated in [1], higher axial forces, in contrast, produce thinner depositions.

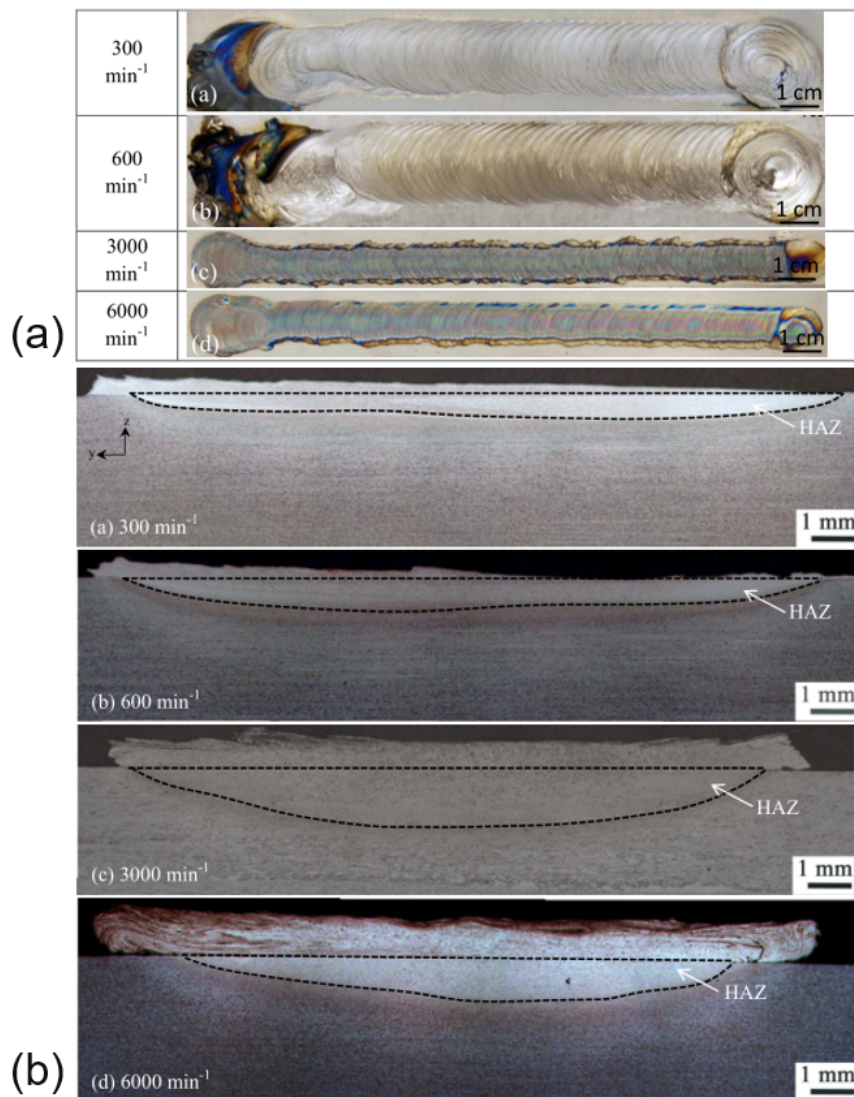


Fig. 3.4: Depositions of Ti-64 with a 20 mm rod. (a) Layers with corresponding rotational speeds; (b) Micrographs of the respective layers [20].

3.1.3 Friction surfacing as an additive manufacturing technique

The process features of FS make it a viable candidate for being a novel additive manufacturing technique. One main reason for this is that the mechanics of the process are based on plastic deformation, which not only helps with avoiding shrinkage defects but also localizes and minimizes the heat input, potentially leading to a decreased part distortion and a small heat affected zone. Additionally, the

process causes no radiation, fumes and spatter, which makes it an environmentally friendly alternative. Especially interesting for additive manufacturing are the easily achievable detailed designs with near net geometry and relatively simple parameter control. On the other hand, some disadvantages are also present. For example, the unbonded edges of the deposition that require post-machining, the generation of a flash that decreases the efficiency and the small number of parameters, which only offers a limited control over the process [3].

Currently, only a few experiments with a multiple layer deposition have been undertaken and solely with aluminium, with a rod diameter wider than 12 mm, as it can be seen in Fig. 3.5. In this example, four layers of AA6082-T6 were deposited on top of each other to achieve a height of 7 mm, being subsequently machined to get a linear rail [3, 22]. Shen *et al.* [23] were also capable of producing a 128 mm long, 18 mm wide and 5.7 mm thick six layer deposition of AA5083 over a AA2024 substrate (Fig. 3.6), where it was shown that the quality of the layers is very reproducible and that the process may be an effective alternative to melting based methods.

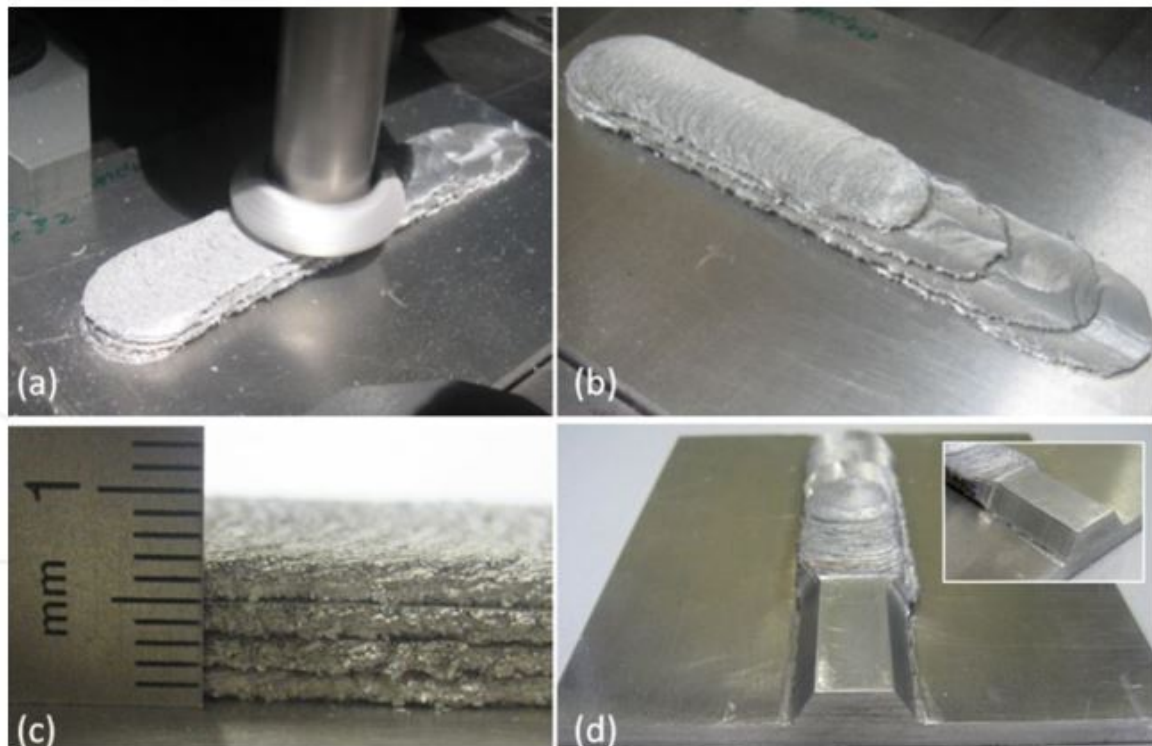


Fig. 3.5: Construction of an AA6082-T6 additive manufactured part with the FS process: (a) multilayer deposition; (b) produced bulk; (c) height of deposition; (d) post machining [3].



Fig. 3.6: Multi layer deposition of AA5083 on a AA2024 substrate produced with the FS process: (a) top view, (b) side view with the individual layers [23].

Further progress has been made by the company MELD, who successfully deposited Ti-64 with a deposition rate of 2.5 kg per hour and was able to construct large parts with solid state additive manufacturing, of which a few examples are shown in Fig. 3.7. They suppressed the formation of the flash by using a hollow rotating tool, as shown in Fig. 3.8, filled with a consumable feedstock and thus increasing the efficiency of the process [24].



Fig. 3.7: Types of structures successfully deposited by MELD [25].

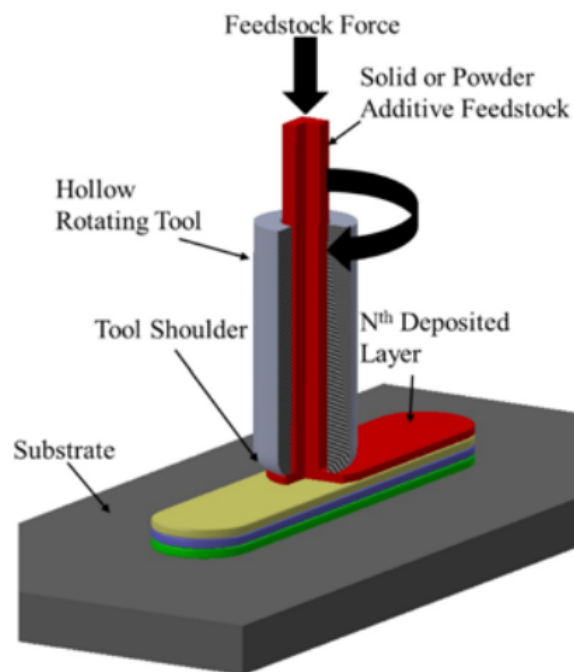


Fig. 3.8: Schematic of the tool used by MELD, with a hollow rotating tool that increases process efficiency by suppressing the flash formation [26].

3.2 Characteristics of titanium alloys

Titanium is besides magnesium and aluminium one of the most commonly used lightweight metals, mainly due to its high strength to weight ratio and high corrosion resistance [27]. The latter is credited to the presence of a passive oxygen layer at the surface, which is highly stable and immediately forms at ambient atmosphere [27]. Generally speaking, Titanium is an allotropic material, which means that it changes its crystal structure with increasing temperature from hcp (α -phase) to bcc (β -phase). This temperature depends on the alloying elements, being around 1000°C for Ti-64 [27]. Moreover, titanium alloys can be divided by the contents of their alloying elements into α -alloys (commercially pure titanium), α - β -alloys (e.g. Ti-64) and β -alloys. [27, 28].

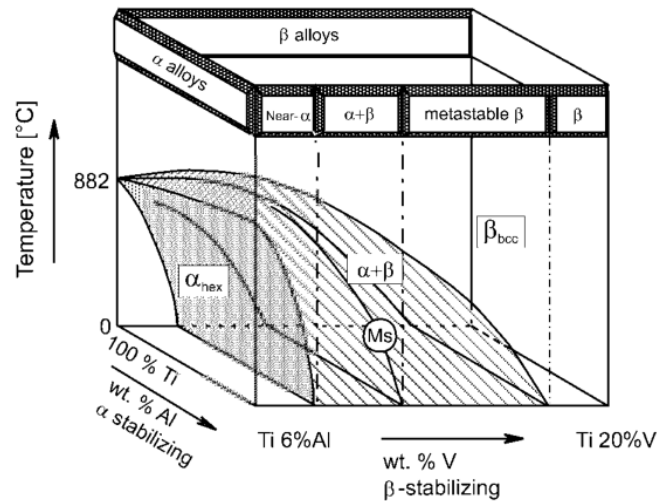


Fig. 3.9: Tridimensional phase diagram with the alloys classified by the wt. % of their alloying elements [28].

3.2.1 α - β -alloys

Among many others, α - β -alloys include Ti-64, which was the one used in the present project. In order to form the two-phase microstructure both α and β stabilizing elements are used. For the α -phase Al, O, N, C are used and for the β -phase the β -isomorphous elements V, Mo and Nb or the β -eutectoid elements Cr, Fe, Si. Therefore, these alloys can exhibit three different types of microstructures. Firstly, the fully lamellar microstructure, which can be obtained by an annealing step in the β -phase field, as shown in Fig. 3.10a. Secondly, in Fig. 3.10b the bi-modal microstructure is visualized, where the cooling rate from the homogenization temperature in the β -phase field plays a crucial role and determines the width of the α -lamellae. Lastly the fully equiaxed microstructure is presented in Fig. 3.10c, which can be achieved with the same heat treatment as for the bi-modal, but with a controlled cooling rate, which needs to be sufficiently low after reaching the annealing temperature in the recrystallization step [27, 28]. These three different types can be seen in Fig. 3.10.

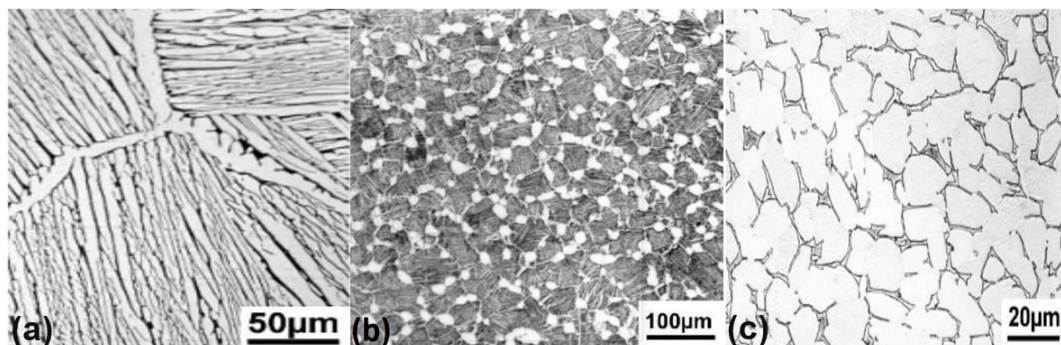


Fig. 3.10: (a) Fully lamellar, (b) bi-modal and (c) fully equiaxed microstructure [27].

3.2.2 Martensite formation in titanium

Generally speaking, martensite is a type of microstructure that forms without diffusion at high cooling rates above a given temperature, called the martensitic transformation temperature. For the case of titanium, this happens upon cooling from the β - to the α -phase, where the onset temperature is 994°C and the required cooling rate being 20 K/s [29]. The microstructure then shows for most Ti-alloys an acicular shape with a hexagonal structure designated as α' , while being supersaturated in β -stabilizers. If the solute contents are increased the hexagonal structure becomes distorted and changes to an orthorhombic microstructure (α'') [27]. This metastable fine plate-like microstructure leads to higher strength and hardness, but this hardening effect is only moderate in comparison to steels [28]. The difference between two heat treatments with different cooling rates from different starting temperatures, explaining this phenomenon, can be seen in Fig. 3.11 [28].

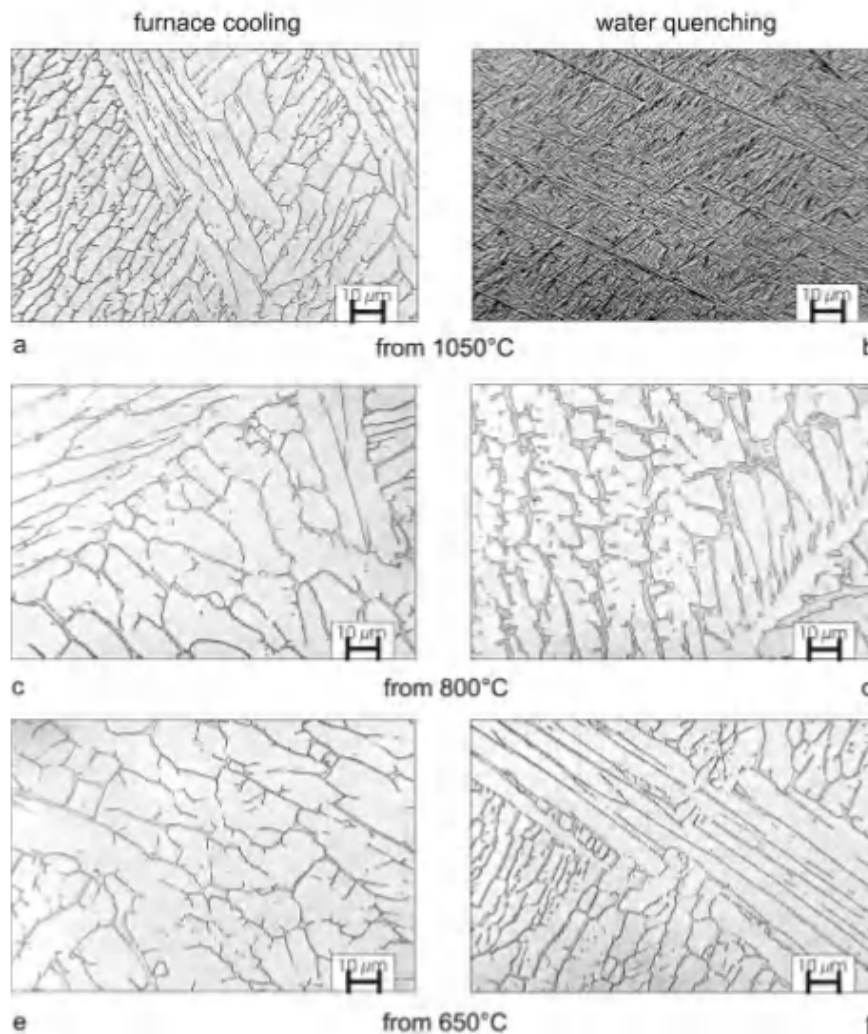


Fig. 3.11: Difference in microstructure caused by the cooling rate for Ti-64. a), c), e) shows a pure lamellar microstructure, achieved with furnace cooling and in b), d), f) the martensite is formed with water quenching [28].

4 Materials and Methods

4.1 Materials

The used material for the rod and the substrate was Ti-64, with the following alloying elements and their corresponding weight percent ranges are shown in Tab. 4.1. The dimensions of the used substrate and rods can be seen in Tab. 4.2. Additionally, in Tab. 4.3 the material properties of Ti-64 are listed.

Tab. 4.1: Alloying elements of Ti-64 according to ASTM B265-20a [30].

Element	Al	V	Fe	O	C	H	Ti	N
wt%	6.2-6.6	3.5-3.9	0.11	0.05-0.15	0.02-0.03	0.0039-0.0049	Bal.	0.007-0.023

Tab. 4.2: Dimension and material of the used substrate and rods.

Component	Dimensions	Material
Substrate	5 mm thickness	Ti-64
Rod	8 mm diameter	
	12 mm diameter	

Tab. 4.3: Material properties of Ti-64 [31].

Property	Value
Density	4.429 mg/m ³
Bulk modulus	153 GPa
Elastic limit	786 MPa
Tensile strength	862 MPa
Thermal conductivity	7.1 W/mK
Thermal expansion	8.7 10 ⁻⁶ /K
Hardness Vickers	349
Melting temperature	1600°C
β -transus temperature	1000°C

4.2 Experimental methods

4.2.1 Friction stir welding machine

For all the single- and double-layer experiments, a I-STIR CNC Series (MTS, United States of America) friction stir welding machine (shown in Fig. 4.1), with the specifications listed in Tab. 4.4, was used. The machine can be operated with either force- or deposition-rate-controlled mode, which means that only the respective parameter is held constant by the machine. Furthermore, since the machine is normally used for friction stir welding, the movement in the z-direction, also called forge depth, is only limited to 19.6 mm, which decreases the maximal achievable length of deposition.

Tab. 4.4: Specifications of the Friction Stir Welding machine.

Process parameter	Max Value
Maximal axial force	30 kN
Maximal rotational speed	3200 min ⁻¹
Forge depth	19.6 mm
Modes	Force and Deposition Control



Fig. 4.1: MTS Friction stir welding machine used in this work.

4.2.2 Choice of parameters and deposition evaluation

For this work three main process parameters were used: rotational speed, axial force and traverse speed. The parameter window for the experiments was initially refined by using the values already obtained from previous experiments for 20 mm rods [20]. Following this, the machine limits were tested by using the minimum and maximum values. The achieved layers were compared to the literature to find out whether it had the characteristics of a successful deposition. With this, a new parameter set was established, tested and compared to the past trials while evaluating the machine feedback, which was the forge feedback, welding time, torque or the deposition rate. The equation to calculate the deposition rate is shown in Eq. 4.1.

$$DR = \frac{z_F * r^2}{t_w} \quad (4.1)$$

With:

- DR ... Deposition rate
- z_F ... Forge movement in the z-direction
- r ... Rod radius
- t_w ... Welding time

This was repeated until a fitting parameter set was found. The same procedure was done for the experiments with the 8 mm diameter rods, as well as for the 12 mm rods, and can be seen as a flow chart in Fig. 4.2.

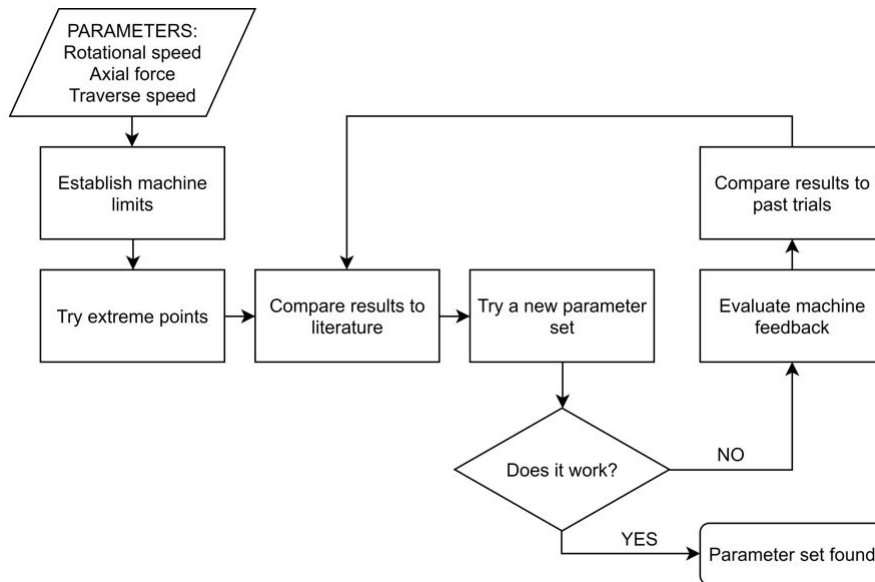


Fig. 4.2: Process of establishing the parameter sets.

In order to evaluate the quality of a layer, certain characteristics were defined as preferable and images, as seen in Fig. 4.3, are added to illustrate the different features. (a) Absence of flash on the layer: The flash should form on the rod and not on the layer. (b) Homogeneity: A continuous deposition with no gaps and constant surface quality. (c) Straightness: Layer should stay in a straight line and not move to the advancing or retreating side. (d) Thickness in the vertical direction should be as high as possible.

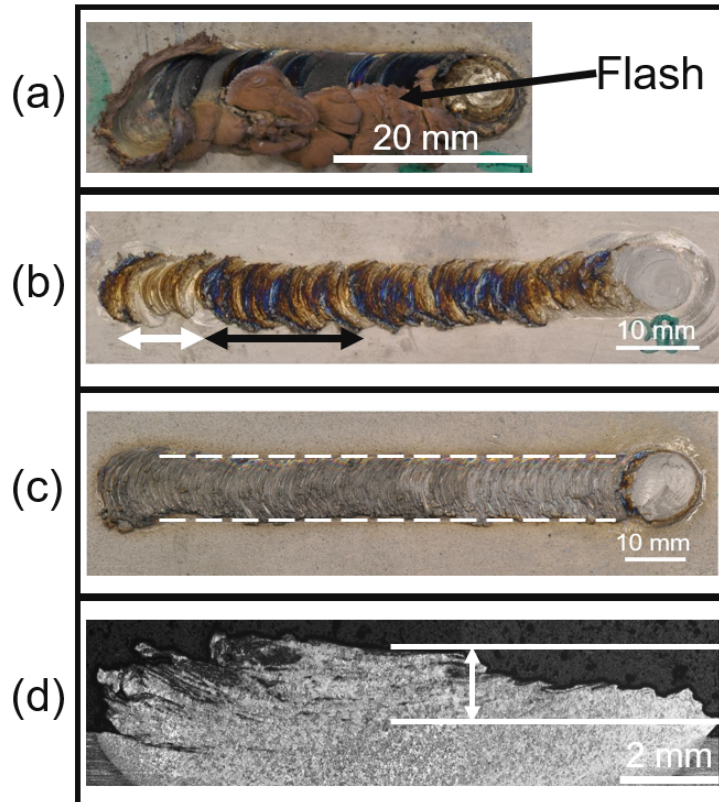


Fig. 4.3: Quality features of the FS process (images are illustrative); (a) Absence of flash on the layer; (b) Homogeneity; (c) Straightness; (d) Thickness.

4.2.3 Temperature measurements

The temperature measurements were done by positioning a 1 mm thick NiCr-NiAl Type K thermocouple (Labfacility, United Kingdom) in a hole drilled through the substrate, with the tip leveled with the surface (see Fig. 4.4).

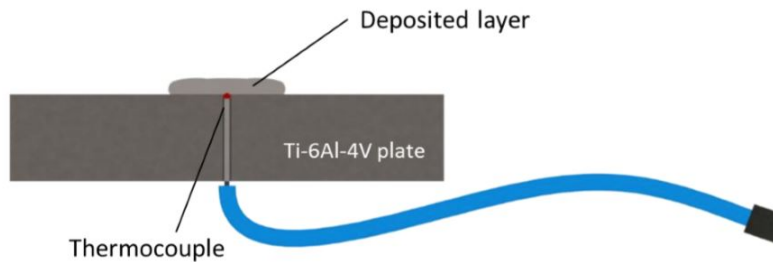


Fig. 4.4: Schematics of the positioning of the thermocouple [32].

Additionally, an infrared camera of the type VarioCAM HD Head (Infratec, Germany), distanced at around 1 meter from the substrate was used. With the emissivity factor for titanium being in a range of 0.75-0.89, corresponding to a temperature range of 800-1300°C, the upper limit of the range was chosen, since temperatures of up to 1300°C were expected [20]. In order to decrease reflections, the substrate was painted black and only the area of the deposition was left out. The camera was positioned as shown in Fig. 4.5.

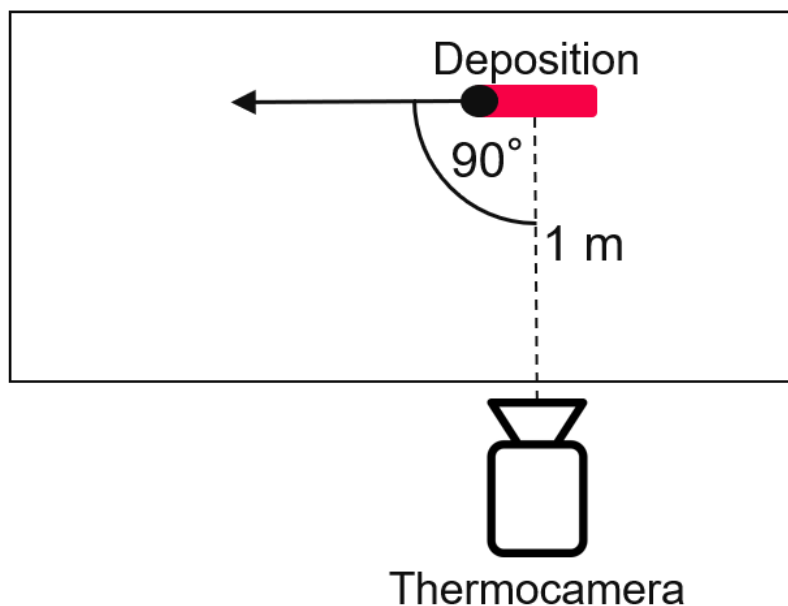


Fig. 4.5: Position of the thermocamera in relation to the deposition.

4.2.4 Hardness tests

The hardness tests were carried out by using a M1C 010 (EMCO TEST, Austria) machine and Vickers Hardness with a force of 0.2 N. The approach for the tests was done by drawing individual hardness lines horizontally across the layer, with evenly distributed testing points. The measuring points were at least separated by 2 times of the diagonal of the indentation, according to ASTM E92-17 [33].

4.2.5 Metallographic preparation

First step of the preparation was to extract and embed the cross-section of the layer. The area where the cross-sections were usually extracted can be seen in Fig. 4.6. This spot was chosen to ensure that the layer had already finished the shortening stage and was in a state of steady deposition.

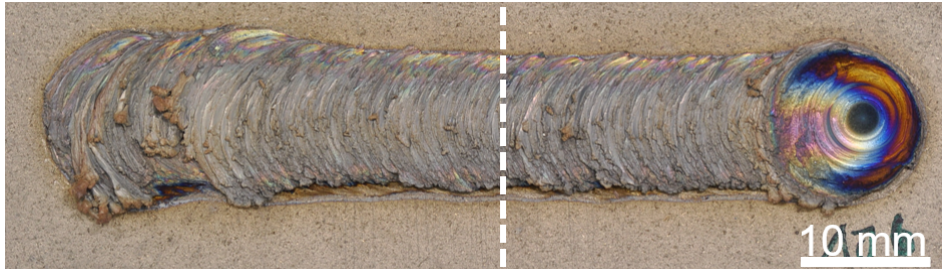


Fig. 4.6: Layer with indicated position of the cut for the cross sections.

After embedding the samples, they were prepared for optical microscopy with the procedure listed in Tab. 4.5 and etched with Kroll's reagent (see Tab. 4.6) for 25s.

Tab. 4.5: Polishing steps used for the metallographic procedure [34].

	Grinding	Polishing	
Type	SiC	Diamond	Colloidal silica
Particle size / μm	320	9	0.04
Rotational speed / min^{-1}	300	150	150
Force / N	15	20	20
Time / min	Until leveled	5	25-30

Tab. 4.6: Solution used for the etching of the cross sections (Kroll's reagent).

HF	HNO ₃	H ₂ O
2 %	4 %	94%

4.2.6 Microstructure characterization

The microstructure was investigated with a Axio Observer Inverted Optical Microscope (Zeiss, Germany) for micrographs and general layer quality observations. To obtain a more detailed look at the microstructure, a Mira-3 Field Emission Scanning Electron Microscope (Tescan, Czech Republic) with a secondary- and a back-scattered electron detector was used.

5 Results and discussion

5.1 Deposition with an 8 mm rod

For these experiments the traverse speed was held constant at 500 mm/min, as the influence on the quality was a minor one and only resulted in stretching and compressing of the deposition patterns along the length of the layer and not in a change of the visual appearance, which can be seen in Fig. 5.1. In [35] it was reported that a change in travel speed only changed thickness and bonded width, but the overall appearance of the deposition kept similar characteristics, which supports the assumption that the traverse speed functions, at these early process development stages, only as a parameter to further optimize minor layer quality features.

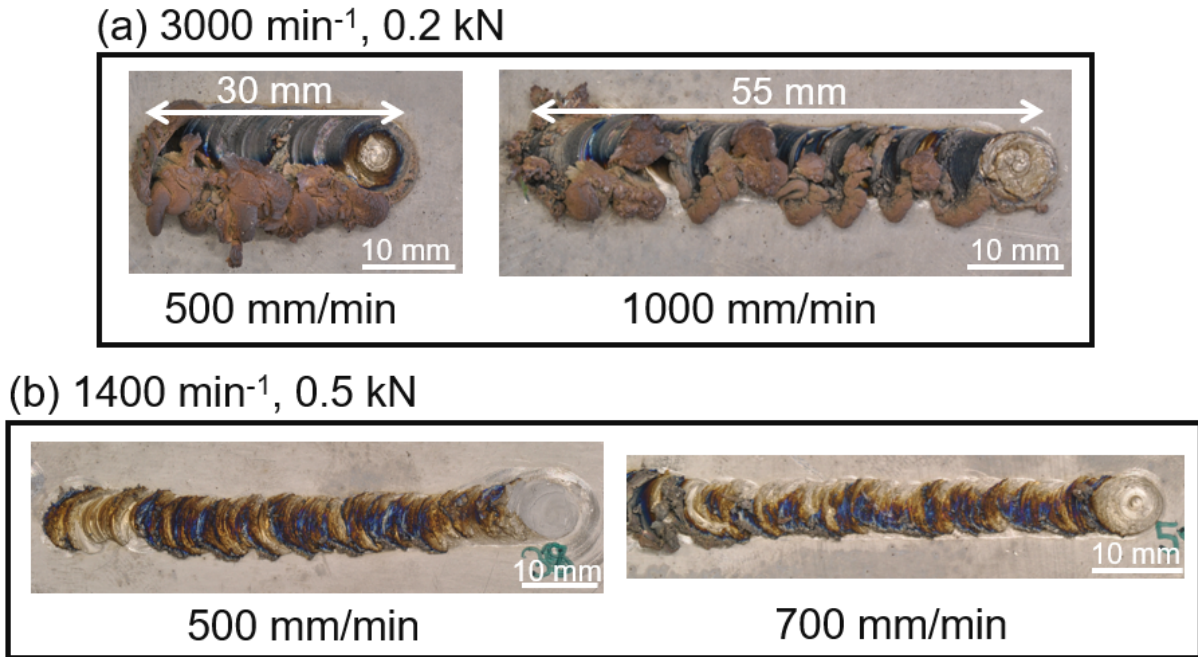


Fig. 5.1: Difference in appearance for depositions with different travel speeds, keeping other parameters constant: (a) 3000 min^{-1} , 0.2 kN, (b) 1500 min^{-1} , 0.5 kN.

As for the shortening stage, the optimal parameters were found by comparing with the data available from the 20 mm experiments [20], being adjusted accordingly considering that a smaller diameter and contact surface would need less force and energy during the shortening stage to plasticize the rod. Therefore, the shortening force was initially decreased by 50% compared to the 20 mm experiments previously published, which readily led to satisfactory results. Aside from shortening stage parameters, parameters ranges were determined according to Fig. 4.2, being presented by Tab. 5.1.

Tab. 5.1: Parameter window for the 8mm experiments.

Process parameter	Parameter range
Axial Force	0.1-1 kN
Rotational Speed	$1200\text{-}3000 \text{ min}^{-1}$
Traverse Speed	600-800 mm/min
Shortening Force	0.5 kN
Shortening Displacement	0.6 mm

Following this, the first step was to evaluate if the force-controlled or the deposition-rate-controlled mode was better suited for a constant and homogenous deposition. The results show that by keeping

the deposition rate constant, large force fluctuations occurred while the deposition-rate-controlled mode and as a result “stop-and-go” patterns were visible (see Fig. 5.2a). This was caused by a sudden increase in force, consequently followed by a reduction, causing insufficient energy input and the breakdown of the shear layer, which in turn hinders material transfer. The main reason for this behavior is probably the unstable flow of titanium around the β -transus temperature [13] and the force feedback of the equipment, not being able to cope with the strong force fluctuations, while using the deposition-rate-controlled mode. Moreover, this difference in deposition quality could be also caused by the “Stick-slip-phenomenon”. This phenomenon describes two surfaces sliding over each other and experiencing a sudden change in force, being caused by overcoming the larger static friction coefficient, followed by the transition to kinetic friction and an increase in velocity [36]. The results obtained from this stage were taken into consideration and therefore only force-controlled mode was used from this point on, where these patterns did not occur.

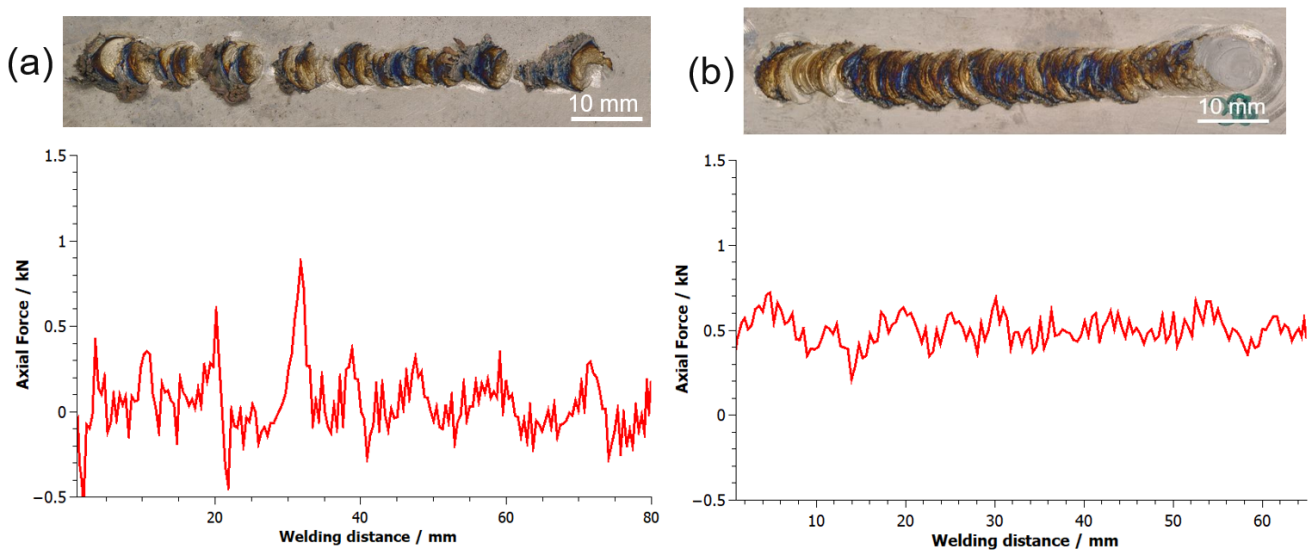


Fig. 5.2: Comparison of depositions with (a) deposition-rate (3000 min^{-1} , $42 \text{ mm}^3/\text{s}$) and (b) force-controlled mode (1400 min^{-1} , 0.5 kN).

After a wide variety of parameter sets were explored, the types of achieved depositions can be divided into three subcategories. Starting with low rotational speeds and axial forces ($<1200 \text{ min}^{-1}$, $0.1\text{-}0.6 \text{ kN}$), Type I is formed, being characterized by having nearly no deposited material. This deposition type is caused by insufficient frictional heat, resulting only in traces of material deposited at the beginning, mainly originated from the plastification that took place during the shortening stage. As the process continued, an immediate breakdown of the viscoplastic shear layer took place, halting the material transfer. No formation of flash was observed (see Fig. 5.3a).

Type II was achieved by increasing the rotational speed to about $1300\text{-}1500 \text{ min}^{-1}$ (Axial Force: $0.2\text{-}0.6 \text{ kN}$). This type could be further split into two subcategories: IIa and IIb. On Type IIa depositions, as shown in Fig. 5.3b, more material was deposited compared to Type I, since the shear layer could be sustained for longer due to the additional heat input, provided by the increase in rotational speed. This phenomenon was also observed by [18, 20].

Within the Type II parameter window, a region between $1300\text{-}1400 \text{ min}^{-1}$ and $0.3\text{-}0.5 \text{ kN}$ resulted in depositions of Type IIa (see Fig. 5.3b). In those depositions, the oxidation layer moved towards the center line of the deposition, showing more material transfer in comparison to Type IIb (see Fig. 5.3c). On those depositions, the characteristic ripple-like features on the surface could be observed, similar to [1, 18, 19, 32, 35]. Furthermore, it must be mentioned that for types IIa and IIb, their respective parameter windows had a considerable overlap, as the process within Type II parameter window demonstrated a high sensitivity to even slight parameter changes [20]. Thus, a clear separation could not be determined.

Lastly, by increasing the rotational speeds above 1600 min^{-1} (0.1-0.6 kN), Type III took place (see Fig. 5.3d). The flash was no longer formed on the rod, appearing instead on the retreating side of the depositions. This caused a large material cluster with strong oxidation. Even though the deposition surpassed Type II in homogeneity and thickness, the presence of a pronounced flash on the deposition made Type III not suitable for further use as a viable parameter window. The formation of this type is probably caused by the excessive rotational speeds and axial forces, which led to high deposition rates (around $300 \text{ mm}^3/\text{s}$). As a result, material flowing towards the retreating side did not have enough time to stick and bond to the surface, instead moving upwards and forming a flash, a phenomenon observed by [35]. Another important factor contributing to this feature is the small rod diameter, which is mentioned by [9], where it was described that the decrease in contact area reduces heat input and gives the deposition not enough time to bond at the substrate and the flash rather moves to the retreating side than to the rod, while the material is pushed outwards by the high pressures.

Beyond Type III, all other experiments with higher rotational speed and axial force led to the same results, meaning excess of deposited material and flash formation on the deposition. Therefore, it could be concluded that a better deposition than Type IIb with this experimental setup could not be reached. The summary of the different deposition types is presented on Tab. 5.2 and Fig. 5.4, which is based on 74 different parameter sets.

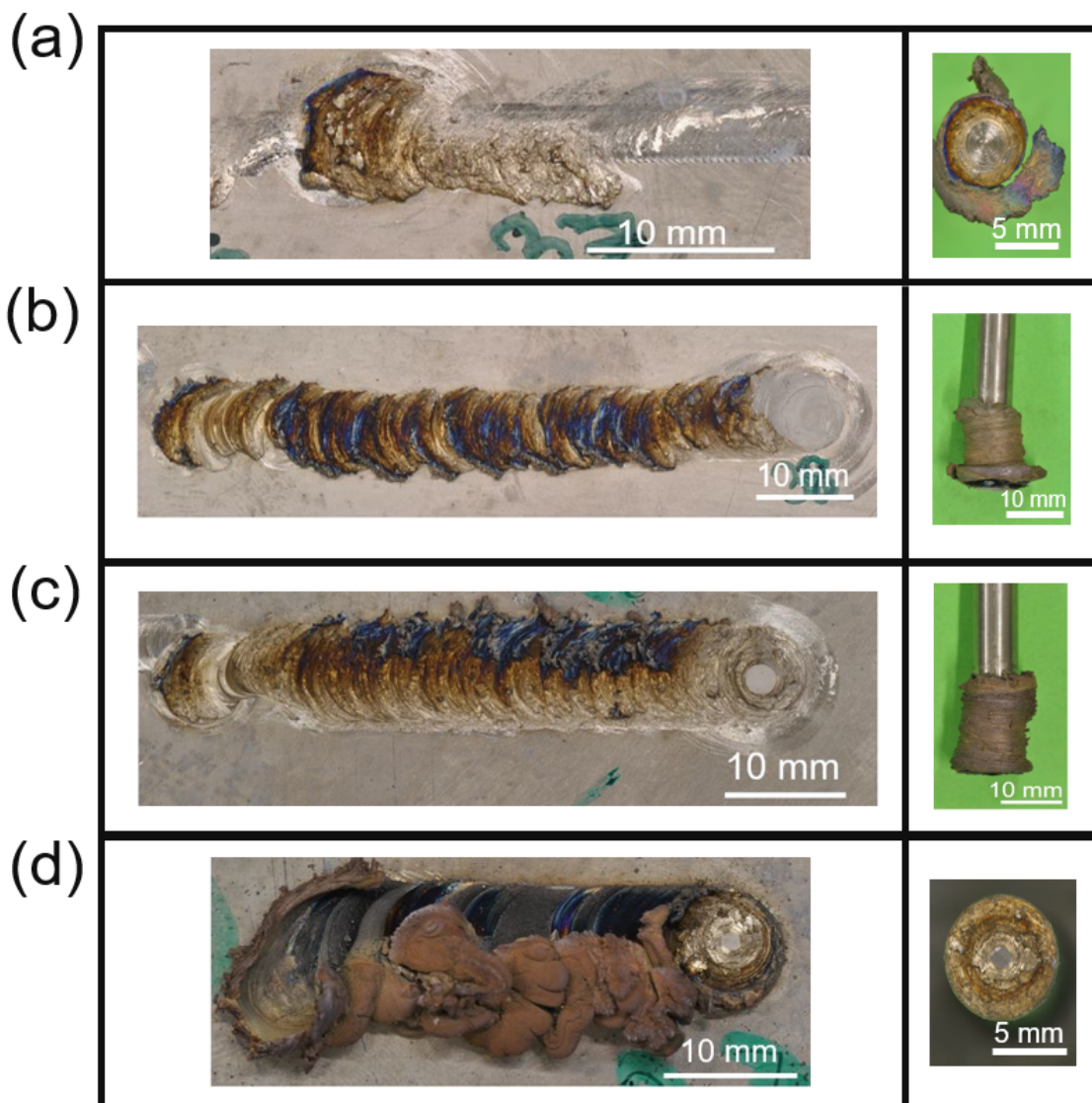


Fig. 5.3: Types of depositions with 8 mm rods and all with 500 mm/min traverse speed. (a) Type I: 1000 min^{-1} , 0.6 kN; (b) Type IIa: 1400 min^{-1} , 0.5 kN; (c) Type IIb: 1500 min^{-1} , 0.3 kN; (d) Type III: 2000 min^{-1} , 0.3 kN.

Tab. 5.2: Parameter ranges for the achieved deposition types.

Type	Rotational speed / min^{-1}	Axial Force / kN	Traverse Speed / mm/min
I	0 - 1200	0.1 - 0.6	500
IIa	1300 - 1400	0.3 - 0.5	
IIb	1300 - 1800	0.2 - 0.6	
III	2000 - 3200	0.1 - 0.6	

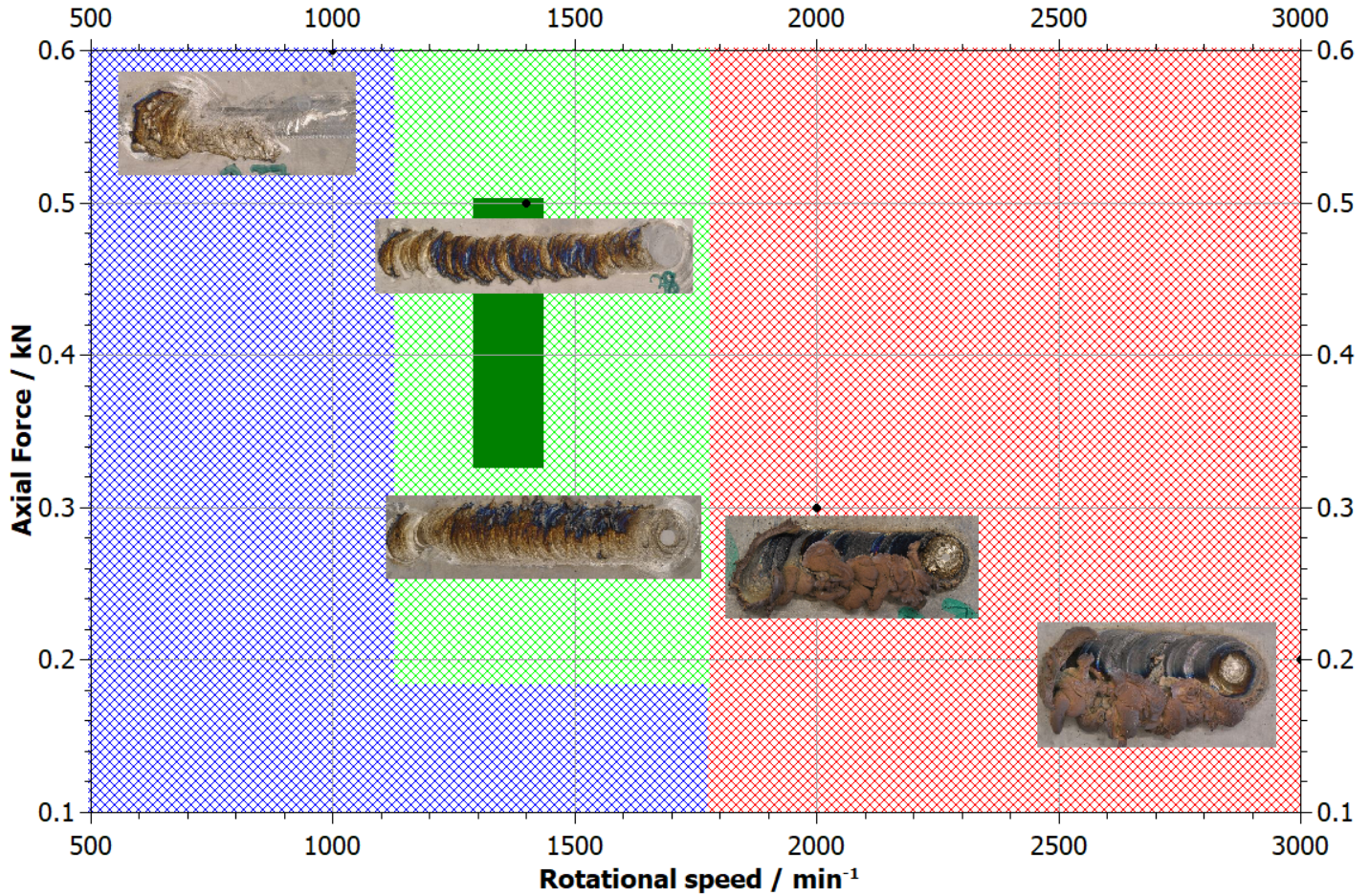


Fig. 5.4: Different types of layers achieved with the 8 mm rod and their corresponding rotational speed, axial force with a constant traverse speed of 500 mm/min. Type I (blue), Type IIa (dark green), Type IIb (green) and Type III (red) are listed.

5.1.1 Microstructural characterization of the 8 mm rod layer

The samples were prepared for optical and scanning electron microscopy, following the steps described in Sec. 4.2.5. The results from the optical microscope can be seen in a micrograph in Fig. 5.5, where also the heat affected zone is indicated (HAZ). Firstly, the microstructure shows some unbonded regions, mainly concentrated on the retreating side (RS). This could be caused by one of the characteristics of the process, which is the deposition always having an offset compared to the center of the rod, consequently leading to a higher temperature on the advancing side [1]. This temperature difference originates from the combination of travelling and rotational speed on the advancing side, causing an increase of energy dissipation by friction [1].

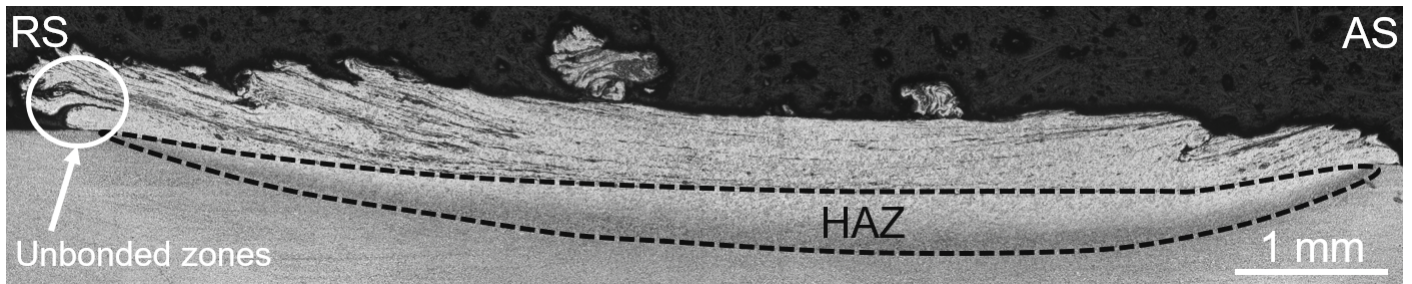


Fig. 5.5: Micrograph of a cross section of the 8 mm deposition with 1400 min^{-1} and 0.5 kN .

On the SEM images in Fig. 5.6, a martensitic matrix is visible, surrounding vortex-shaped clusters of α -phase grains, which in turn were observed either surrounding or around pores. This microstructural feature has been observed elsewhere [17], being the exact origin for its formation still unknown. The authors of the mentioned publication proposed two different hypotheses to the phenomenon. The first hypothesis is the formation of shear bands, which are formed upon reaching temperatures above 1100°C and strain rates greater than 10 s^{-1} , conditions which are fulfilled during the FS process (see Fig. 5.7). Those regions tend to concentrate a large density of dislocations, which in turn would decrease the activation energy for the nucleation of α -phase upon cooling, leading to groups of small grains (around $1 \mu\text{m}$) appearing in morphologies that resemble material flow patterns. The presence of pores (visible on Fig. 5.6 as dark spots) is also a characteristic of well-developed shear bands [37].

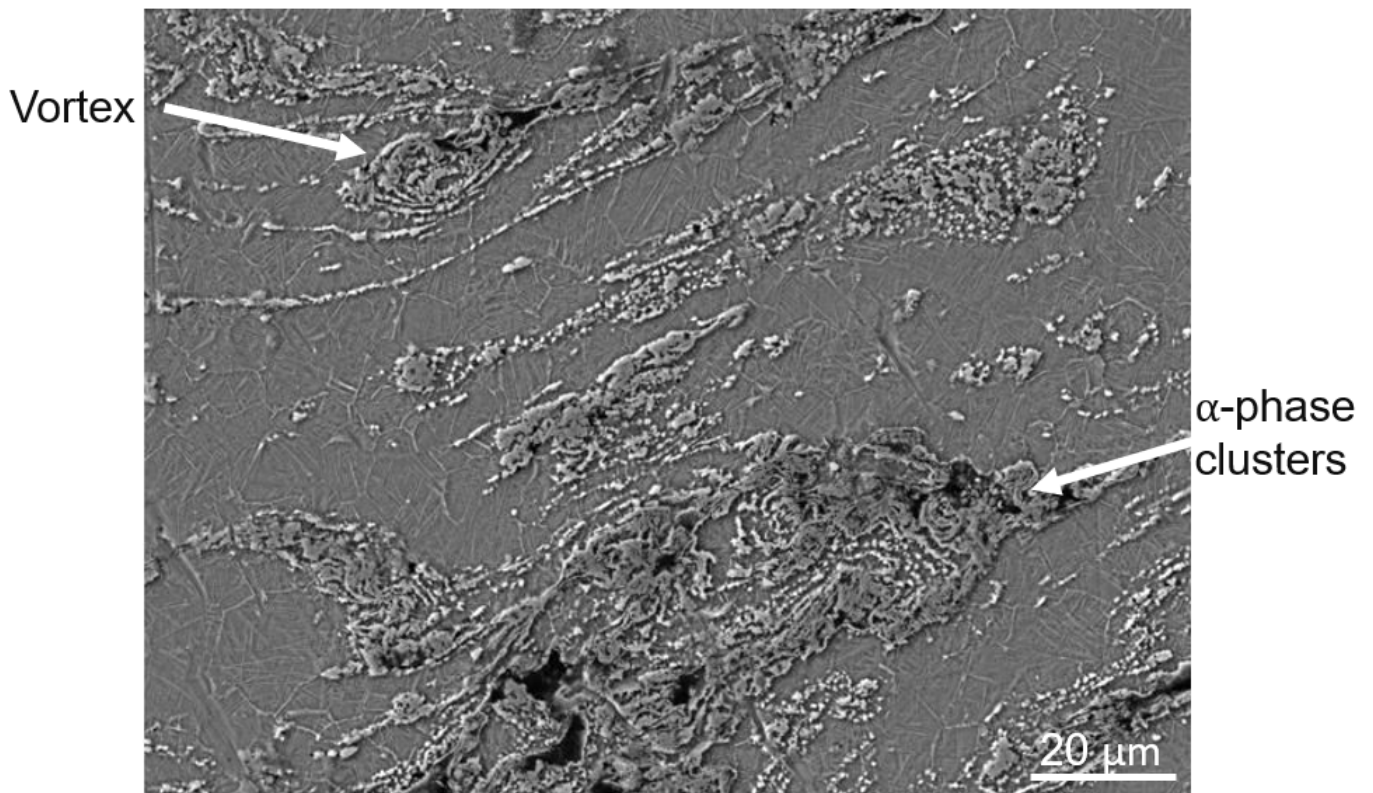


Fig. 5.6: SEM images of the cross section of a deposition with an 8 mm rod (1400 min^{-1} , 0.5 kN).

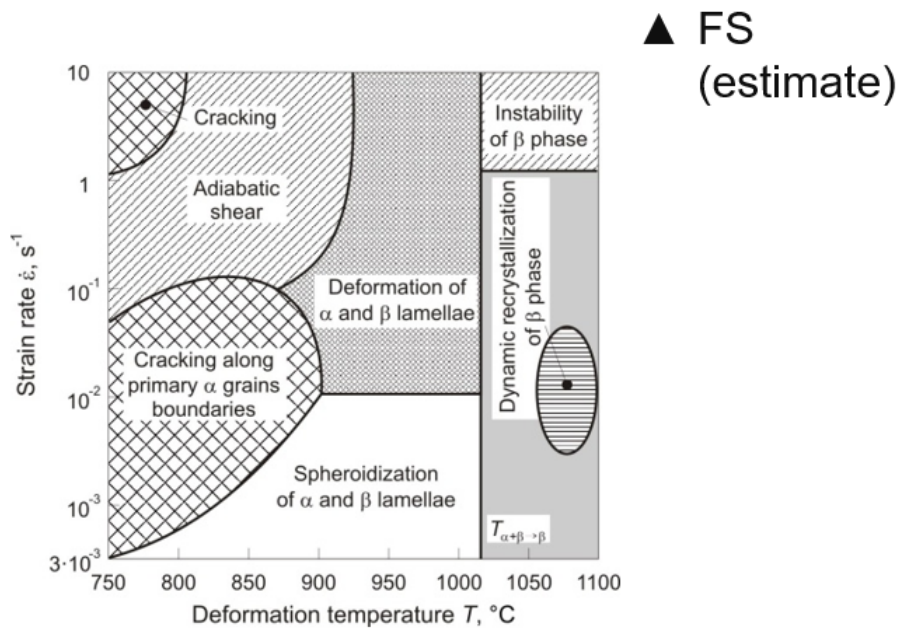


Fig. 5.7: Map of microstructural changes occurring during hot processing of Ti-64. Black triangle estimates the position of the FS as a process relative to the diagram. Adapted from [38].

Another hypothesis proposed by the authors of [17] takes into account the stabilization of α -phase by the presence of oxygen on the surroundings. The so-called α -case, formed on exposed regions of hot-deformed parts processed under uncontrolled atmosphere [27], may form in this case at the edges of the shear layer, being immediately mixed during the material transfer, which would explain the observed vortex/flow shape. The presence of pores could also be explained by this hypothesis, since the mixed α -case does not deform as easily as the β -phase [27], making the material flow more difficult. A definitive explanation to this phenomenon, which accounts for virtually all the porosity on FS coatings, is still to be obtained.

Therefore, it can be concluded that the depositions achieved with 8 mm show porosity, which can be attributed to the used forces not being high enough to close the pores. Even if one would increase the axial forces to counteract this, the layers would shift to Type III and as a consequence would not be usable for double-layer depositions.

5.1.2 Hardness tests of the 8 mm depositions

For the hardness tests of the deposition, a single line of 15 testing points was done (see Fig. 5.8) and for the substrate and rod, 10 evenly distributed measurements were performed on their individual cross-sections. As stated by [7] and [20], the hardness does not change significantly in the vertical direction and therefore one singular horizontal line at the center should be representative for the whole layer. The hardness curve with corresponding hardness values can be seen in Fig. 5.9.



Fig. 5.8: Position of the hardness line on an 8 mm rod deposition.

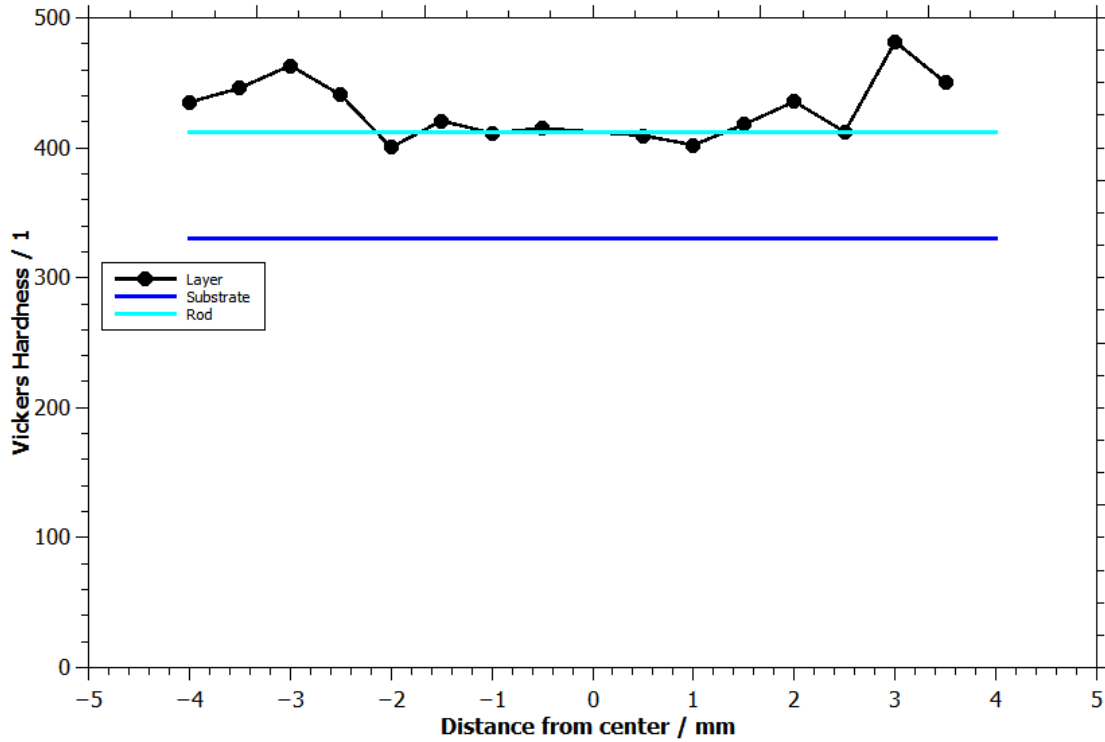


Fig. 5.9: Hardness values for the 8 mm rod deposition in relation to the distance from the center.

The results from the hardness tests show a hardness increase at the advancing and retreating sides in comparison to the rod. This may be explained by the formation of α -case at the edges of the layer [16], as mentioned before. This behavior has been also observed elsewhere [32]. Moreover, extruded rods tend to be harder than hot-rolled sheets, a tendency that is maintained after the rod material is transferred to the deposition [27].

5.2 Depositions with a 12 mm rod

After having limited success with 8 mm rods the diameter was increased by 50% to improve the stability of the viscoplastic layer and provide a larger contact surface. This larger contact surface also meant that higher rotational speeds would be required, since more energy would be needed to plasticize the material. Therefore, the rotational speed and axial force for an ideal deposition was estimated to be 50% higher, assuming a possible linear dependence between rod diameter and required rotational speed. Due to the increase in diameter by 50%, it was suspected that the increased bonding time would also favor a higher traverse speed, which therefore was increased until satisfactory results were achieved (an increase of around 40% was sufficient). Due to the similar phenomenon mentioned in Sec. 5.1, the traverse speed was kept constant after that. With this strategy and the gained knowledge from Sec. 5.1, the parameter window was less challenging to estimate and can be seen in Tab. 5.3.

Tab. 5.3: Parameter window for the 12 mm rod experiments.

Process parameter	Parameter range
Axial Force	0.2-1 kN
Rotational Speed	1400-3200 min^{-1}
Traverse Speed	600-1000 mm/min
Shortening Force	0.5-1.2 kN
Shortening Displacement	0.6-1 mm

In order to obtain a homogenous deposition with rods of larger diameter, the shortening stage needed to be adjusted. The initial trials with the parameters obtained from the experiments with 8 mm rods resulted in a wider spread plastification stage, which normally should be localized at the initial starting point of the deposition and be finished before the travel speed is applied (see Fig. 5.10).

Therefore, in order to provide more energy for the initial shear layer consolidation, force and displacement during the shortening stage were raised until satisfactory results were achieved, which occurred after force and displacement were increased by 140% and 60%, respectively, in comparison to 8 mm experiments. This adjustment stage also considered past experiments and available literature for 20 mm [20].



Fig. 5.10: Impact of insufficient energy input during the shortening stage on the layer quality; 0.7 kN shortening force and 1.0 mm displacement.

As a general trend, the 12 mm depositions showed a more homogenous appearance with less oxidation as well as an increase in thickness, which can be seen in Fig. 5.11 and 5.12. Moreover, it was only possible to achieve depositions of Type I and Type II, which were already mentioned for 8 mm, since the equipment is only capable of rotational speeds up to 3200 min^{-1} and more energy is needed to reach the temperatures necessary for the flash to move to the substrate (Type III). This occurs in contrast to the results from 20 mm [20], where similar deposition types occurred, but the flash formed at the substrate for lower rotational speeds. Therefore, it can be suspected that the decrease in diameter and increase in pressure stops the flash from moving upwards and instead bonding it to the retreating side, which means that the parameter sets with rotational speeds greater than 3000 min^{-1} would lead to a flash free layer if the diameter would be increased, giving the material more time to flow in the upwards direction. The parameter windows and corresponding layers established by 35 different parameter sets and trials can be seen in Fig. 5.13 and Tab. 5.4.



Fig. 5.11: (a) Deposition with a 12 mm rod and (b) corresponding flash; 3000 min^{-1} , 0.5 kN, 800 mm/min.

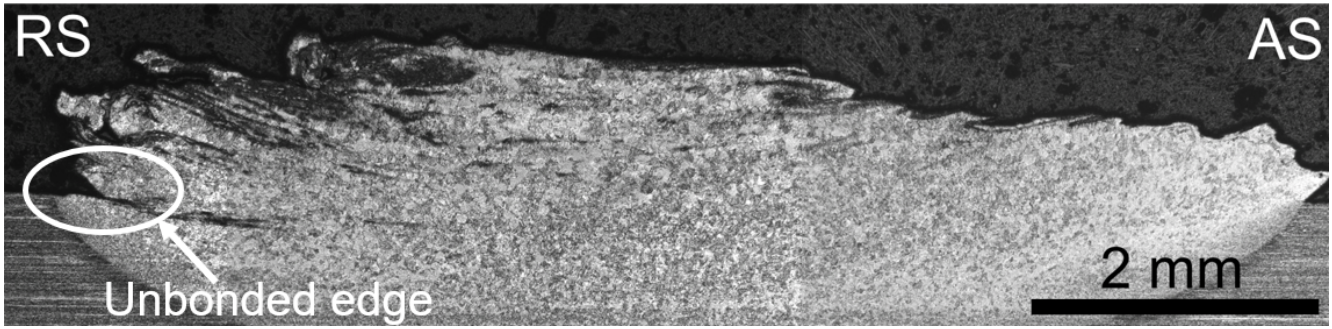


Fig. 5.12: Micrograph of a deposition with 3200 min^{-1} and 0.8 kN . In comparison to the 8 mm deposition the thickness is increased to 1.3 mm at the center. The layer shows unbonded edges on the RS but not on the AS.

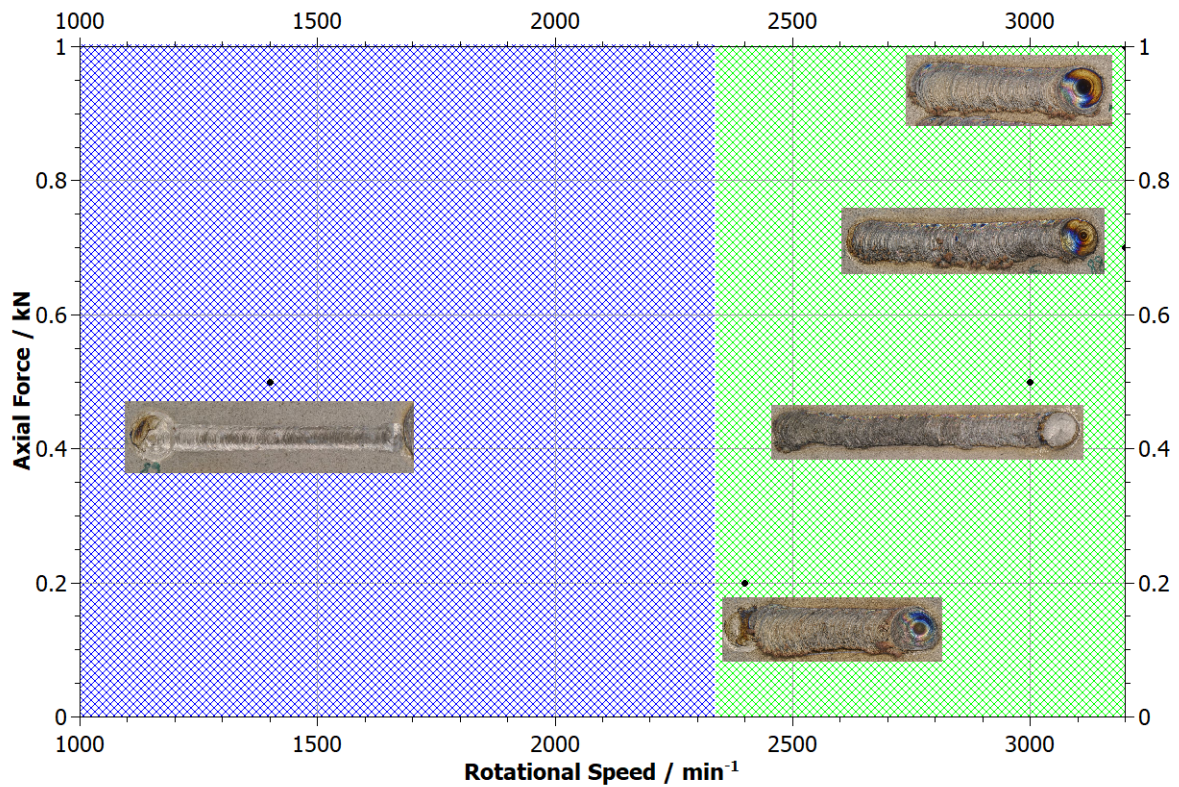


Fig. 5.13: Different types of layers achieved with the 12 mm rod and their corresponding rotational speed, axial force, and a constant traverse speed of 700 mm/min . The areas for Type I (blue) and Type II (green) can be seen.

Tab. 5.4: Parameter ranges for the achieved deposition types with 12 mm rods.

Type	Rotational speed / min^{-1}	Axial Force / kN	Traverse Speed / mm/min
I	0 - 2300	0.1 - 1	700
II	2400 - 3200	0.2 - 1	

5.2.1 Influence of force on the layer appearance

As reported by [22] and [35], normally an increase in axial force leads to an increase in bonded width and energy consumption, but to a decrease in thickness (for a particular combination of rotational and traverse speed). Since there is no literature available that describes the impact of force for FS of

titanium, an attempt to obtain an insight into this topic was made, by keeping the rotational speed and travel speed constant and observing the change in layer quality for various axial forces. Therefore, six different trials were done with a constant rotational speed of 3200 min^{-1} and 700 mm/min travel speed, which led to the best depositions in terms of visual appearance in former trials. The results can be seen in Fig. 5.14.

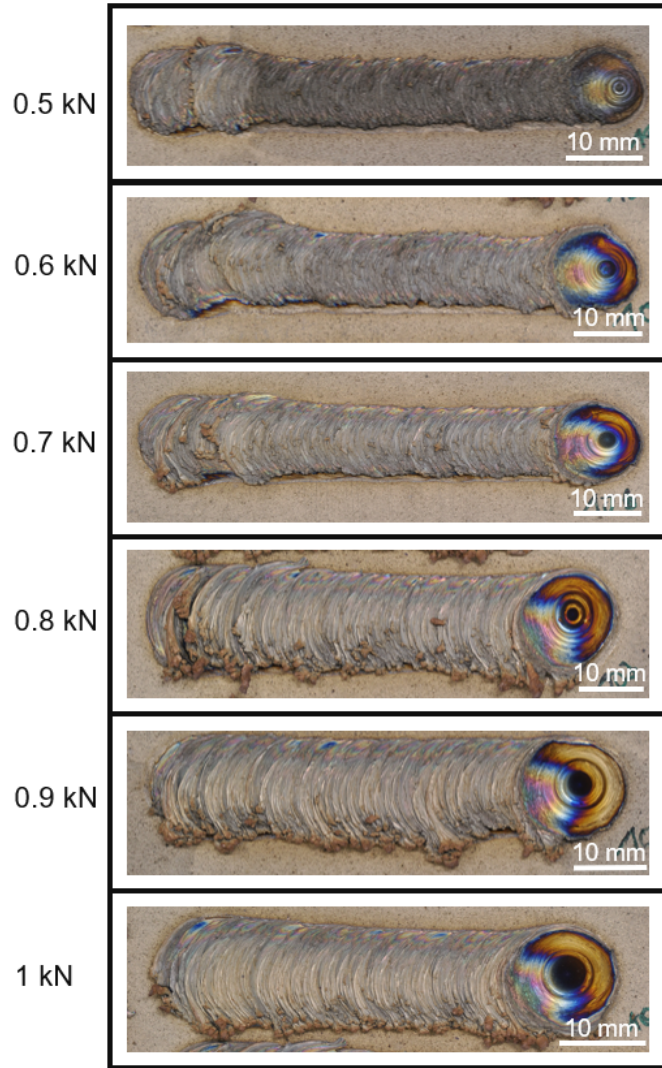


Fig. 5.14: Impact of the force on the visual appearance of a 12 mm deposition. Force is varied from 0.5 to 1 kN, while rotational speed and travel speed are kept constant.

It appears that the higher forces tend to soften the material even more, pushing out the plasticized material to both the retreating and advancing side. This increase in force led to a slightly wider spread deposition, which is supported by [35]. At around 0.8 kN the flash starts to form at the retreating side. To get further insight into the influence of axial force on the resulting layer appearance, the energy input during the process would need to be calculated with the equation for specific energy (Eq. 5.2) from [35]. The equation calculates the mechanical power provided by the equipment by incorporating the power from the rod rotation, axial force and travel speed. This equation does not give a value for the actual energy input, only the power provided by the machine, since modelling for FS is still scarce. However, this equation provides values that can be used to draw reasonable comparisons between different conditions.

$$\dot{W}_e(J/s) = \dot{W}_r + \dot{W}_z + \dot{W}_x = \frac{2\pi\Omega}{60}(T_1 - T_0) + F_z V_z + F_x \nu \quad (5.1)$$

For this calculation, the terms \dot{W}_z and \dot{W}_x can be disregarded, since the plunging speed V_z and the force in x-direction F_x are negligible in comparison to the other terms, only having a small contribution to the applied power

$$\dot{W}_e(J/s) = \frac{2\pi\Omega}{60}(T_1 - T_0)$$

With:

- \dot{W}_e ... Mechanical power supplied by the equipment
- \dot{W}_r ... Mechanical power regarding rod rotation
- \dot{W}_z ... Mechanical power regarding axial force
- \dot{W}_x ... Mechanical power regarding travel speed
- T_0 ... Torque of the freely rotating rod
- T_1 ... Torque of the rod plunging to the substrate
- $F_{z,x}$... Force in z- and x-direction
- ν ... travel speed

With \dot{W}_e and the deposition rate (DR) the energy consumption per mass (EC) can be calculated by assuming that the joining efficiency is 100% :

$$EC (J/kg) = \frac{\dot{W}_e}{DR} \quad (5.2)$$

In this case, instead of using the deposition rate as way to express mass flow, only the volumetric deposition rate DRvol with the unit mm^3/s was used. Then the formula changes to:

$$E_{spec}(J/\text{mm}^3) = \frac{\dot{W}_e}{DRvol} \quad (5.3)$$

With this formula (Eq.5.3), the specific energy in relation to the force could be calculated and plotted in Fig. 5.15.

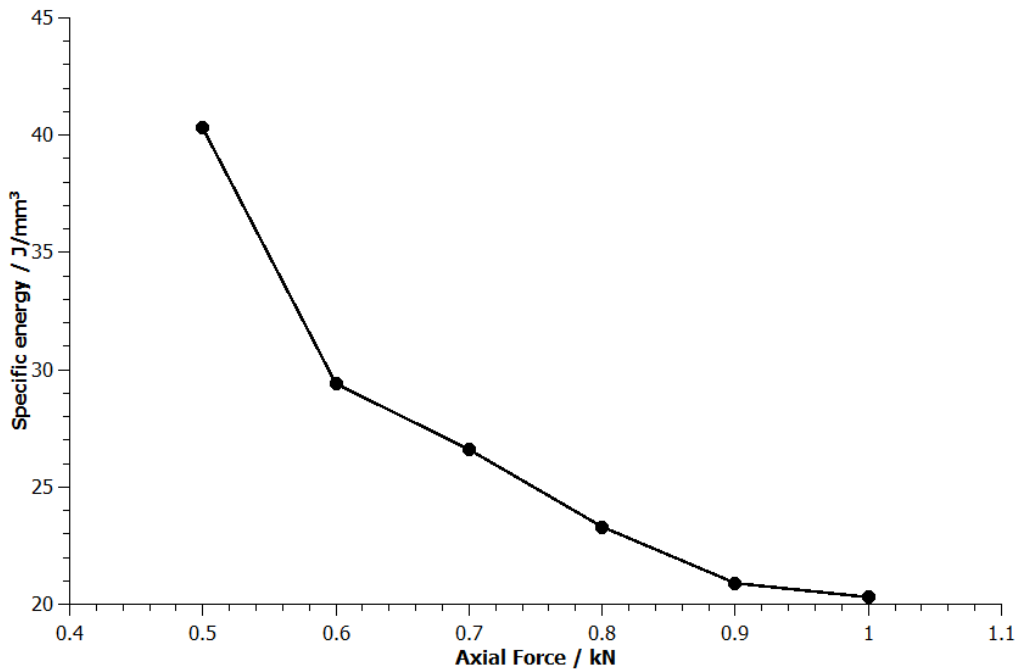


Fig. 5.15: Change of Energy Input per volume for different axial forces.

This curve shows that by increasing the axial force with constant rotational speed, the specific energy decreases, which could stem from the higher forces increasing the temperature and softening the material, therefore decreasing the energy and torque needed for sustaining the deposition process. So the hypothesis can be drawn that a Type II deposition reaches its force-consumption “threshold” at 0.5 kN and a further increase leads to wider spread deposition with less energy needed to sustain the process.

5.2.2 Temperature measurements

5.2.2.1 Thermocouple

By using the method described in Sec. 4.2.3 a temperature measurement for a 12 mm rod single-layer was obtained by using the parameter set 3200 min^{-1} , 0.5 kN and 700 mm/min. The position of the thermocouple and the corresponding micrograph can be seen in Fig. 5.16.

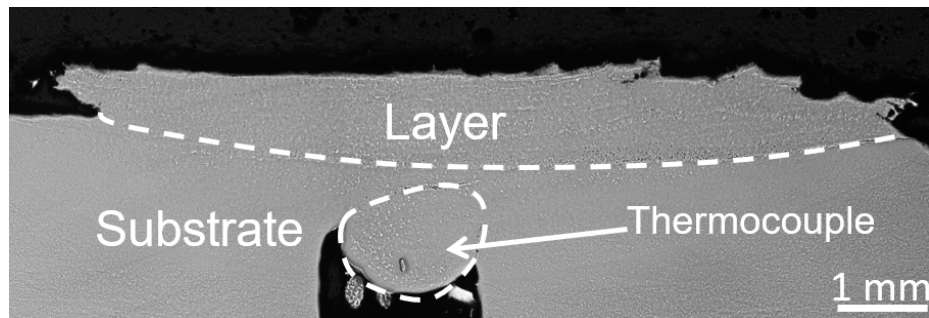


Fig. 5.16: Position of the thermocouple in the cross section. It is visible that the thermocouple is welded with the layer.

During the deposition, the thermocouple reached a temperature of 1160°C (Fig. 5.17), nearly the same as the 1169°C reported for 20 mm [20], which lies above the β -transus point of 1000°C [27], but below the melting temperature of 1600°C [27]. The observed martensite (see Fig. 5.6) was formed due to the high cooling rate (600 K/s within the first 10 seconds after the deposition), which according to [27,29] is above the threshold (20 K/s) for the formation of this microstructure.

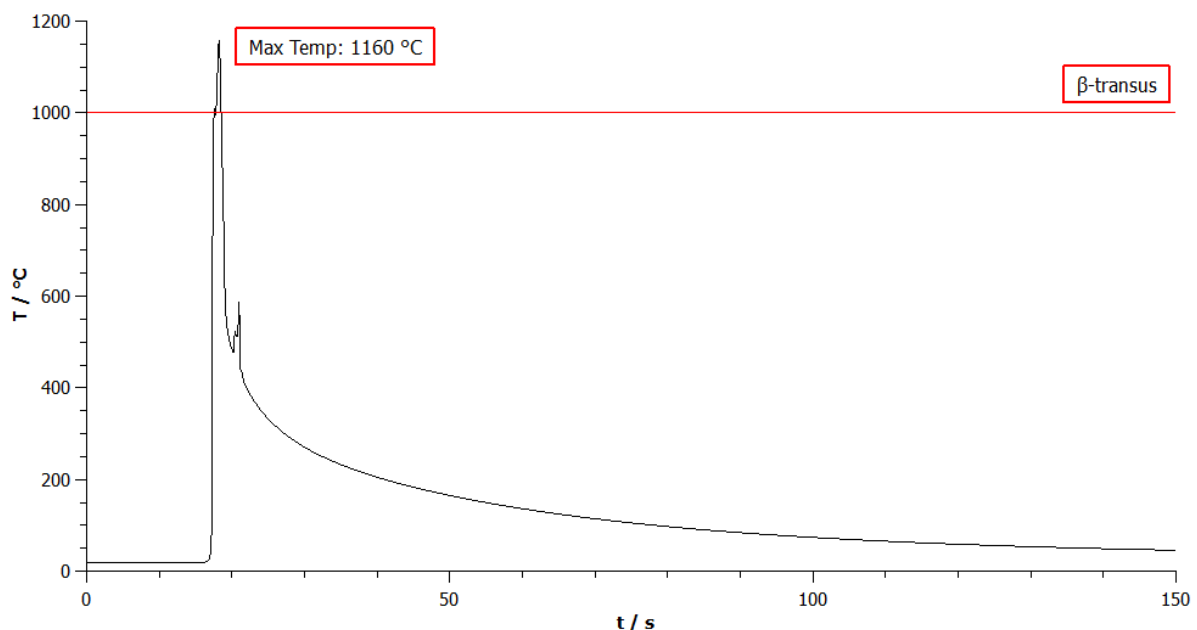


Fig. 5.17: Temperature curve achieved by the thermocouple experiment, with the indicated maximum and β -transus temperature.

5.2.2.2 Infrared camera

In order to obtain more information about the temperature gradients above the substrate, for example on the flash and on the shear layer, a thermocamera was used and the results can be seen in Fig. 5.18. In this case the maximum temperature amounts to 1280°C and is not reached at the tip of the rod, but instead on the rubbing interface further above on the rod [4]. This region exhibits the highest temperature, due to the viscous slipping, which is caused by the speed difference between the rod and deposited layer, resulting in this interface being the most significant heat source of the process [4,35]. In order to show this a temperature line was drawn and plotted in Fig. 5.18. Compared to the results from the thermocouple measurements, the maximum temperature is 120°C higher, since the thermocouple can only measure the temperature underneath the layer and is not able to detect the “true” temperature maximum at the rubbing interface. Moreover, the measured maximum temperature is almost identical to the one reached with 20 mm [20].

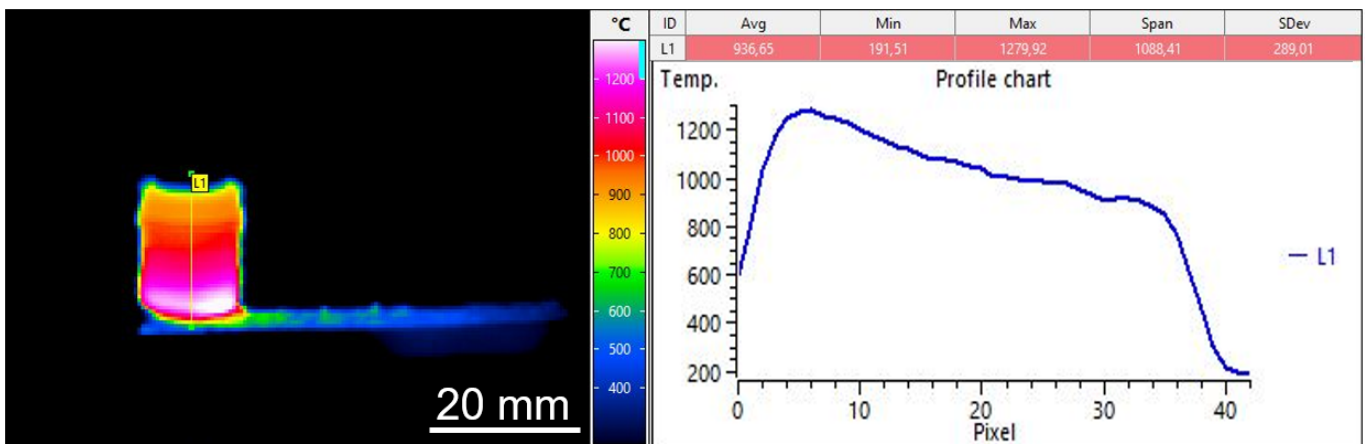


Fig. 5.18: Thermocamera measurement at a distance of 1 meter and with an emissivity factor of 0.89.

5.2.3 Hardness tests of the 12 mm rod depositions

For the hardness tests of the 12 mm depositions a similar approach as for the 8 mm was taken. 3 horizontal measuring lines with 9 evenly distributed measuring points were drawn. The location of these lines and the corresponding hardness values can be seen in Fig. 5.19 and 5.20.

The results show that at the bottom of the layer the hardness was similar to the rod, while in the middle the hardness had a slight increase, which was not significant. Lastly, at the top of the layer (3rd row) the hardness once again increases pronouncedly. This may be ascribed to the formation of oxygen stabilized α -grains, which tend to be harder [27], as mentioned in Sec. 5.1.1.

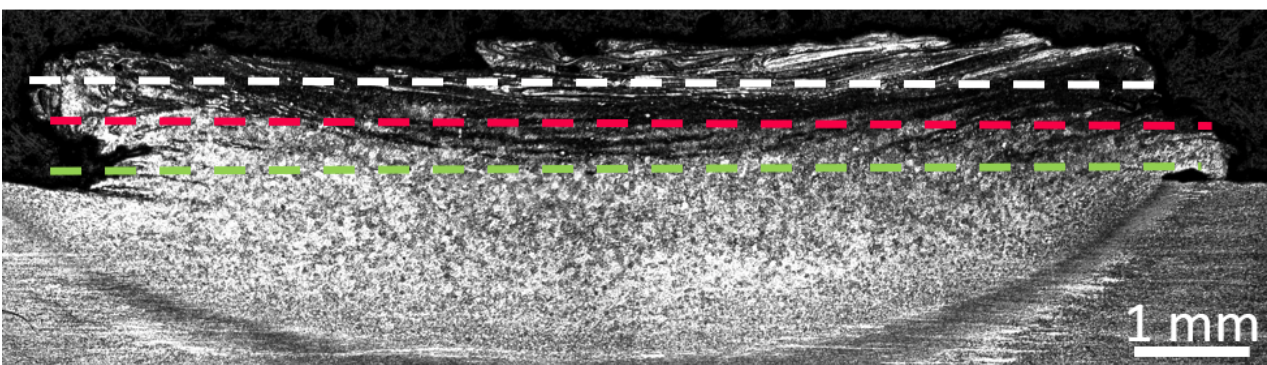


Fig. 5.19: Position of the measuring lines for the 12 mm single-layer deposition.

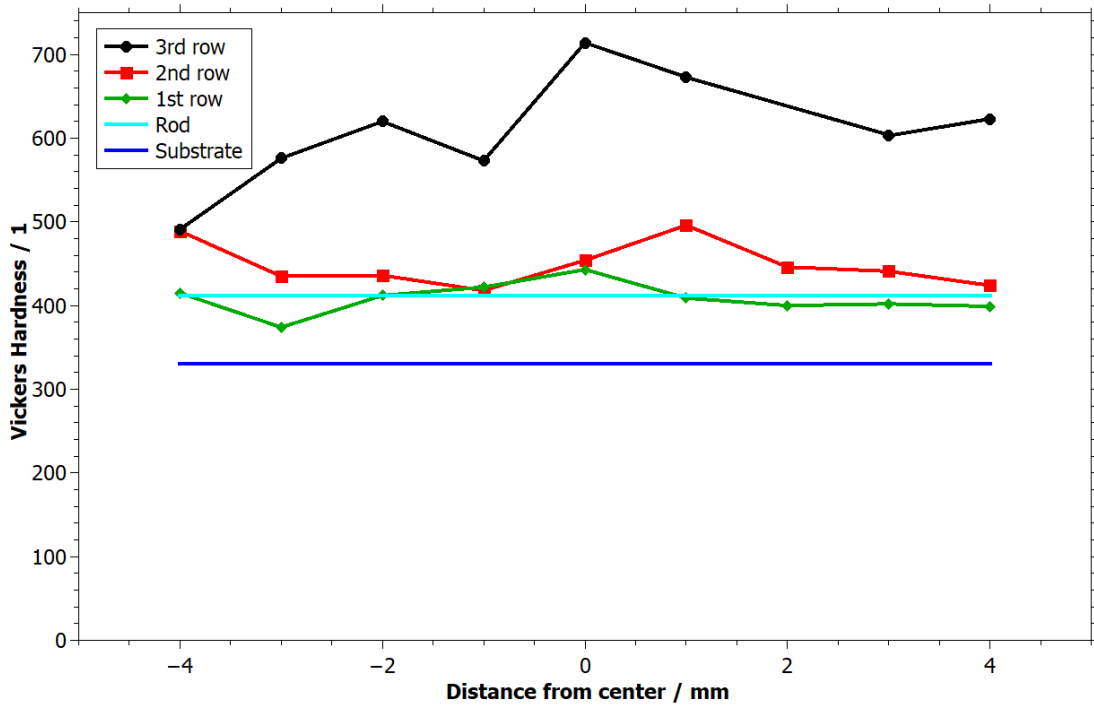


Fig. 5.20: Hardness values of the single-layer in relation to the distance from the center.

5.2.4 Influence of rod diameter on the layer formation

Now by achieving a constant deposition for both 8 and 12 mm rods a comparison with 20 mm is necessary. Therefore, the best depositions in terms of visual quality, where the flash formed on the rod are shown in Fig. 5.21.

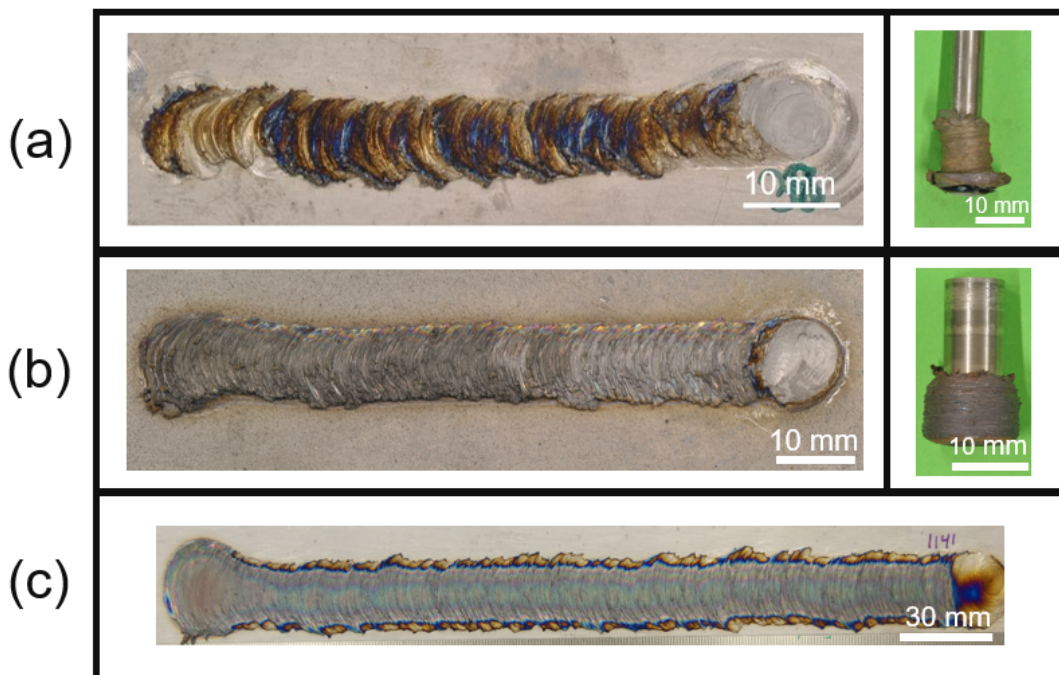


Fig. 5.21: Best possible depositions for 8 mm (a) 1400 min^{-1} , 0.5 kN and 500 mm/min); (b) 12 mm, 3000 min^{-1} , 0.5 kN and 800 mm/min); (c) 20 mm (adapted from [20]), 3000 min^{-1} , 2 kN and 960 min^{-1} rods.

By observing the visual appearance of all three layers, it becomes clear that the 8 mm deposition strongly differs in terms of homogeneity and absence of oxidation. In order to compare the energy consumption for the different rod diameters, the specific energy was derived for the layers with 8, 12 and 20 mm rods (see Fig. 5.22), using the method explained in Sec. 5.2.1. The graph shows that the consumed energy is the same for 8 and 20 mm rods but for 12 mm it is increased, forming an upside-down U-shaped curve. This is a direct result from the measured torque, the main factor on Eq. 5.2, which exhibited the same tendency (see Fig. 5.22).

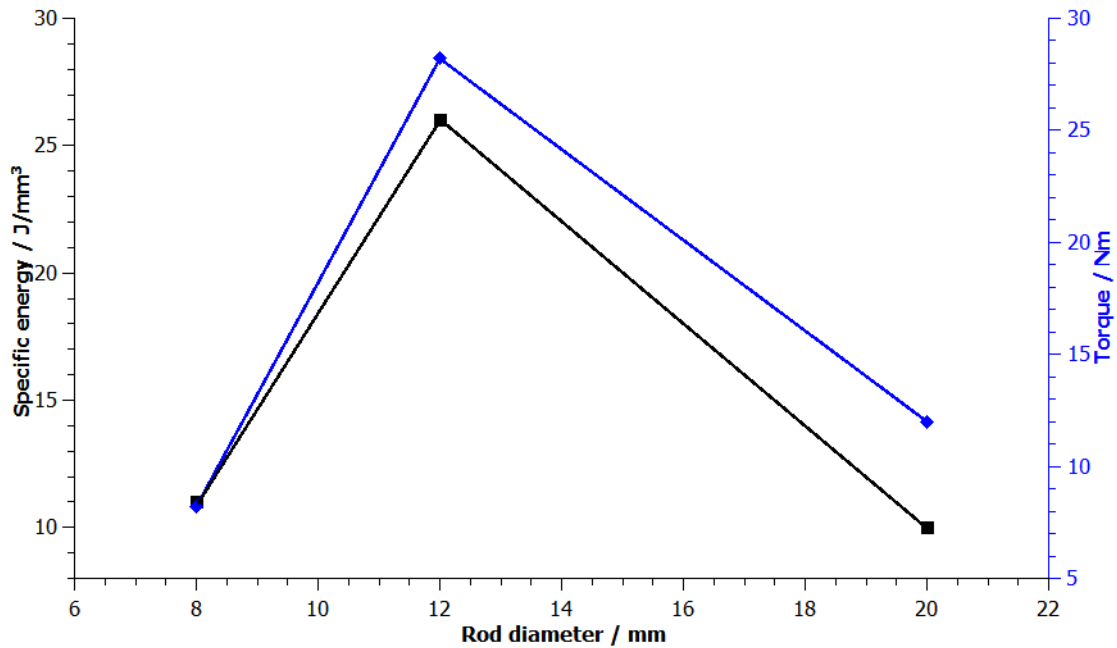


Fig. 5.22: Specific energy and torque in relation to the rod diameter.

The increase in torque when increasing the rod diameter from 8 to 12 mm is expected, since the torque is proportional to the rod radius [39, 40]. However, the decrease in torque between experiments with 12 mm and 20 mm would at first glance deny this hypothesis, since in such a case the torque should increase even further. However, its actual decrease may be ascribed to an increase in contact area, which generates more heat by friction, leading to a softer rod tip, as it was shown for the case of friction stir welding, where an increase in tool diameter led to an increase in temperature [40]. As a result of a softer material, the energy consumed to sustain the deposition is decreased, which is translated to a smaller torque.

Therefore, combining both hypotheses, the rod diameter appears to have two different, combined effects on the measured torque (and consequently on the specific consumed energy) during the FS process: one directly and other inversely proportional. The directly proportional component is the one purely related to the rotation of a rigid cylinder of a given radius around its axis of revolution, with not only its own moment of inertia, but also the friction against the substrate acting against the movement [39]. The inversely proportional component takes into the consideration that as the rod diameter is increased, softening of the material sets in, decreasing the required torque for the revolution [40]. The critical rod diameter would be the point where the torque is maximum, and beyond which the latter component overcomes the former one. A hypothetical and only illustrative visualization of the combination of effects is presented by Fig. 5.23. However, it is important to reiterate and emphasize that the explanation provided here to the observed phenomenon is based only on hypotheses, and as such could only be tested with further experiments, which go beyond the scope of the present project.

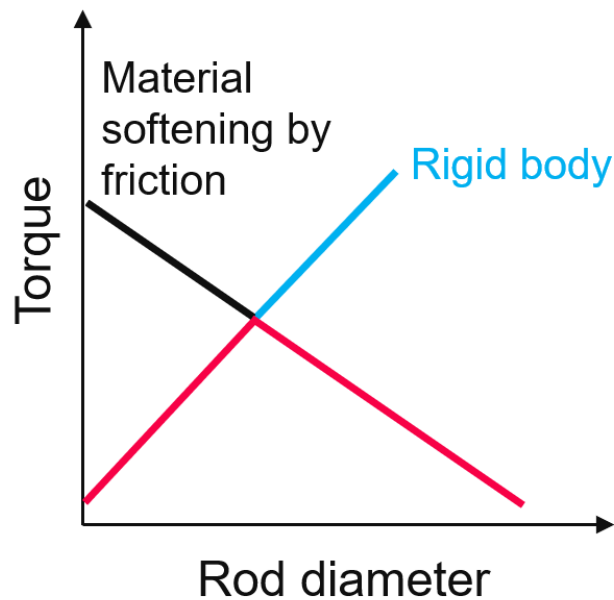


Fig. 5.23: Illustrative presentation of the model explaining the relation between torque and rod diameter.

5.3 Double-layer deposition with a 12 mm rod

In order to establish the feasibility of the process as an additive manufacturing technique, the results from 12 mm experiments were used to create a double-layer deposition, since the results from 8 mm were deemed as not appropriate for multi-layer stacking. The approach for the double-layer deposition was to deposit a single-layer with the optimal parameter set, and then to add a second layer centered on top of the first layer. However, to counteract the offset to the advancing side [1], the tip of the rod was centered slightly to the retreating side. Moreover, no milling steps were applied between layers, and an unused rod with no flash was used for the second layer.

Due to the decreased contact surface between the layers caused by the ripple-like features of the FS depositions, an adjustment of the shortening stage was needed, as a means to increase the energy input for the formation of the initial shear layer. However, even though the displacement of shortening stage was increased to 1.5 mm (50% higher than the single-layer deposition), still 80% of the whole layer was taken up by the stretched shortening stage.

To counteract this more data about the shortening stage, as well as a piece of equipment with a higher displacement in the z-direction would be required to produce longer, more stable and homogenous double-layer depositions. However, in spite of the present limitations, a double-layer deposition, seen in Fig. 5.24, was successfully deposited.



Fig. 5.24: Example of a double-layer achieved with a 12 mm rod (2nd layer in the white dotted line). 1st layer: 3200 min⁻¹, 0.5 kN, 700 mm/min; 2nd layer: same as 1st layer but displacement of the shortening stage was altered to 1.5 mm.

5.3.1 Microstructural characterization of the double-layer

To obtain information about the microstructure and formation of the double-layer a micrograph was made and can be seen in Fig. 5.25. The second layer is centered on the middle of the first with the same general microstructure but the transition zone on the advancing side differs from the surrounding microstructure, which indicates that at this state a seamless transition between consecutive layer is not achieved.

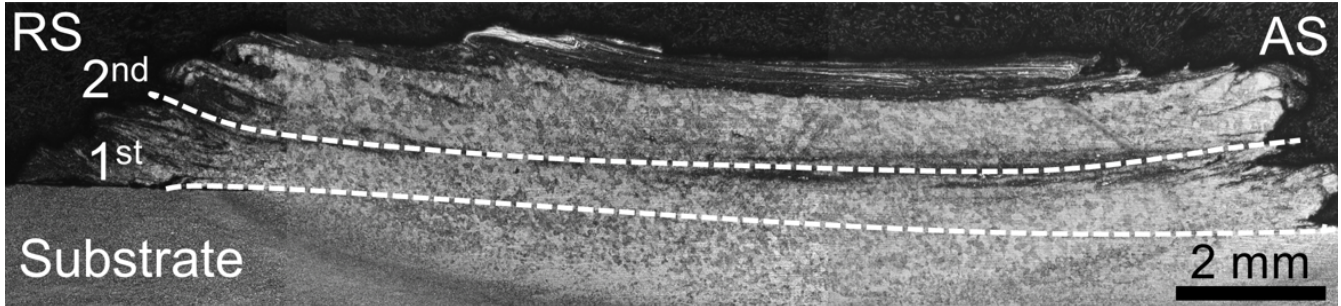


Fig. 5.25: Micrograph of a cross section of the 12 mm rod double-layer deposition.

Furthermore, the microstructure of the two layers was compared in Fig. 5.26 and by calculating the average grain size an enlargement in the second layer (see Fig. 5.26c) in comparison to the first (see Fig. 5.26b) could be detected ($d_I = 85 \mu\text{m}$ and $d_{II} = 100 \mu\text{m}$). This increase could stem from the fact that the presence of the first layer between the second one and the substrate decreases the heat dissipation, since the solid area through which heat can flow by conduction is limited to the surface of the layer underneath. With lower heat dissipation, the cooling rate is lower, which enables recrystallized grains to grow further. This is not the case for a single-layer deposition, which is in direct contact with the substrate, enabling a higher heat dissipation and consequently a higher cooling rate.

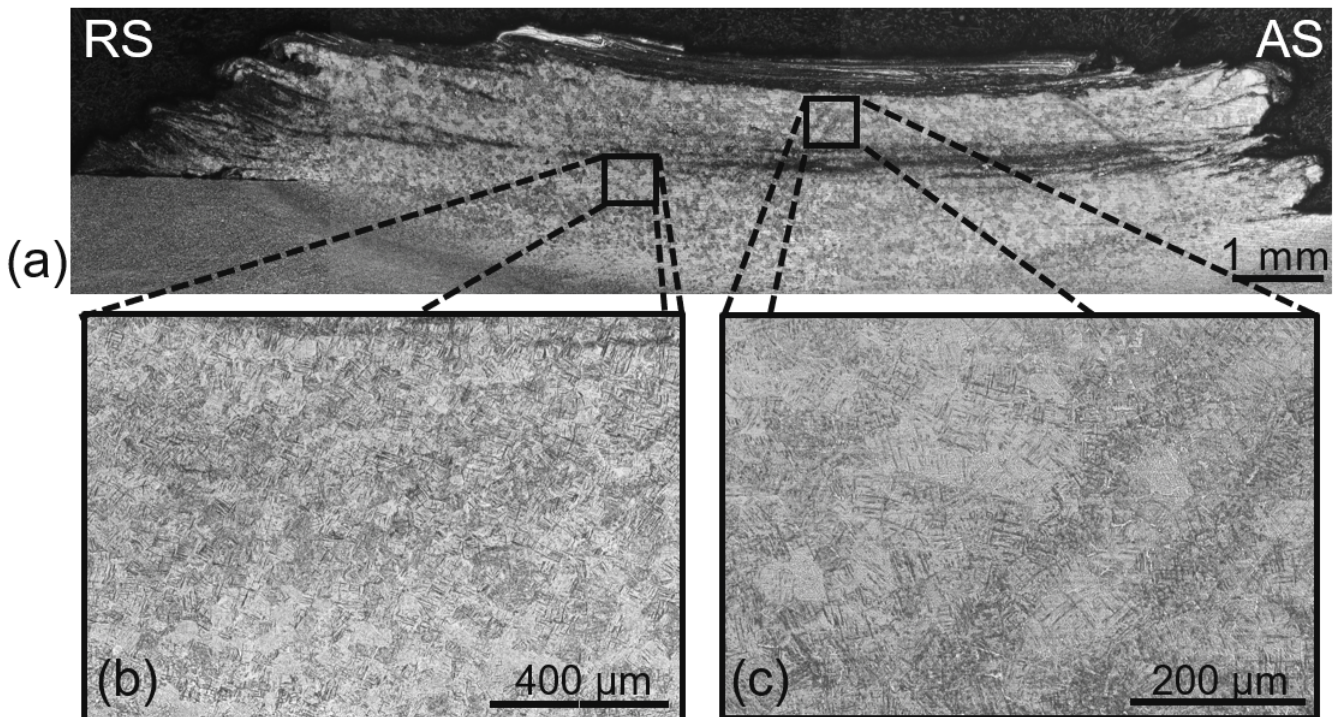


Fig. 5.26: (a) Micrograph of the double-layer with detailed images from the (b) first and (c) second layer.

Additionally, to evaluate the layer quality the cross sections were taken to the SEM and the results can be seen in Fig. 5.27.

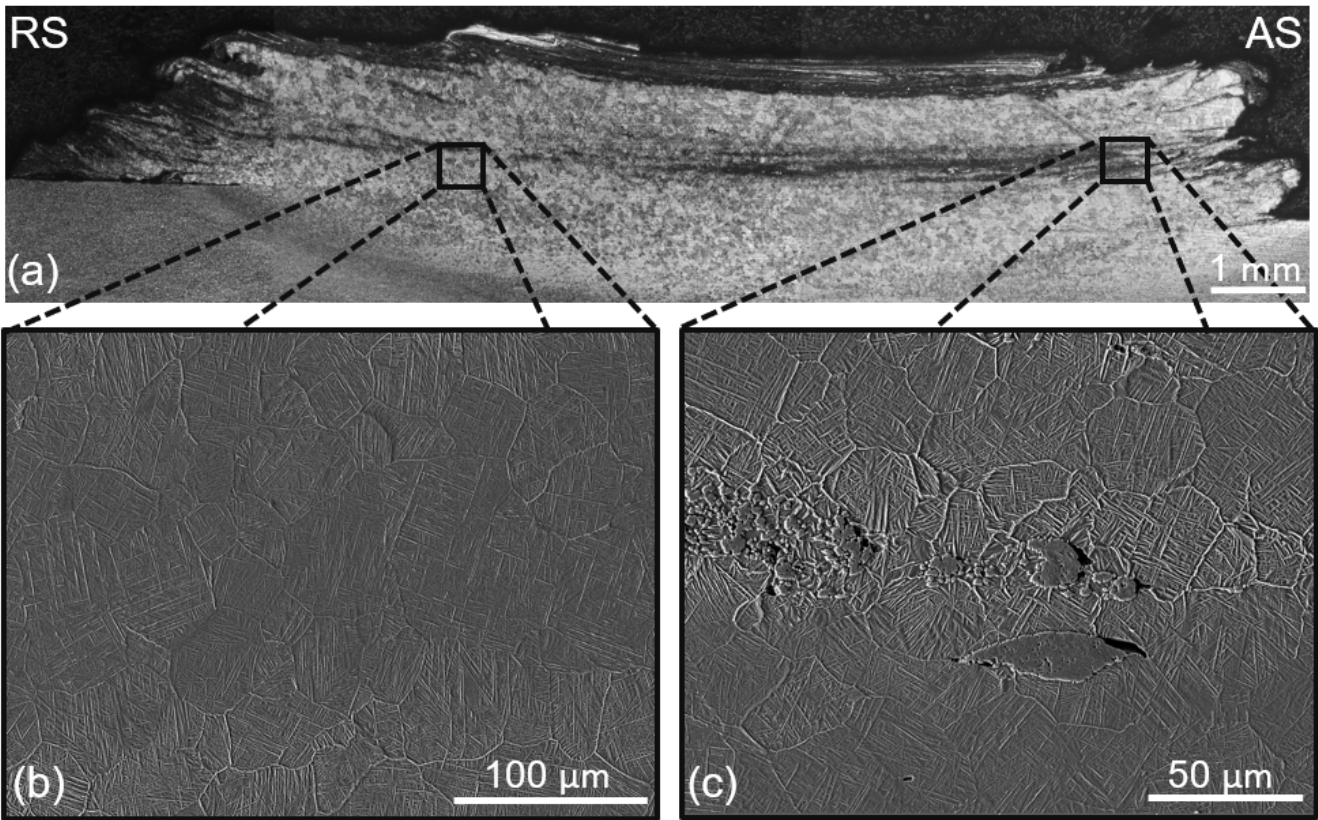


Fig. 5.27: Micrograph (a) with SEM images from retreating side (b) showing the martensitic matrix and advancing side (c) with pores (visible as dark spots) and the presence of α -grains.

The images show that, as expected from the temperature measurements in Sec. 5.2.2, a martensite matrix is present for both layers, in more detail for the first layer in Fig. 5.27b, despite the lower cooling rate that possibly took place during the deposition of the second layer. The α -phase is found again at the shear bands in the interface between the two layers and is shown in Fig. 5.27c, as mentioned in Sec. 5.1.1. Also it became apparent that at the interface some porosity is present, surrounded by small α -grains, which is similar to the phenomenon mentioned in Sec. 5.1.1 [38].

5.3.2 Hardness tests of the double-layer

For the double-layer hardness tests the exact same procedure was done as for the single-layer deposition for 12 mm rods, which consisted of 3 three measuring lines with 9 hardness indentations were obtained and the positions as well as the values are shown in Fig. 5.28 and 5.29

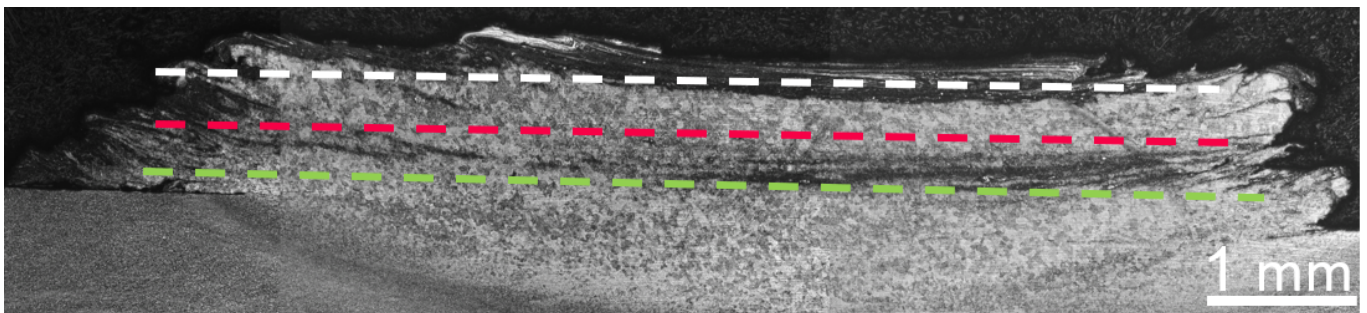


Fig. 5.28: Position of the hardness lines for the double-layer deposition.

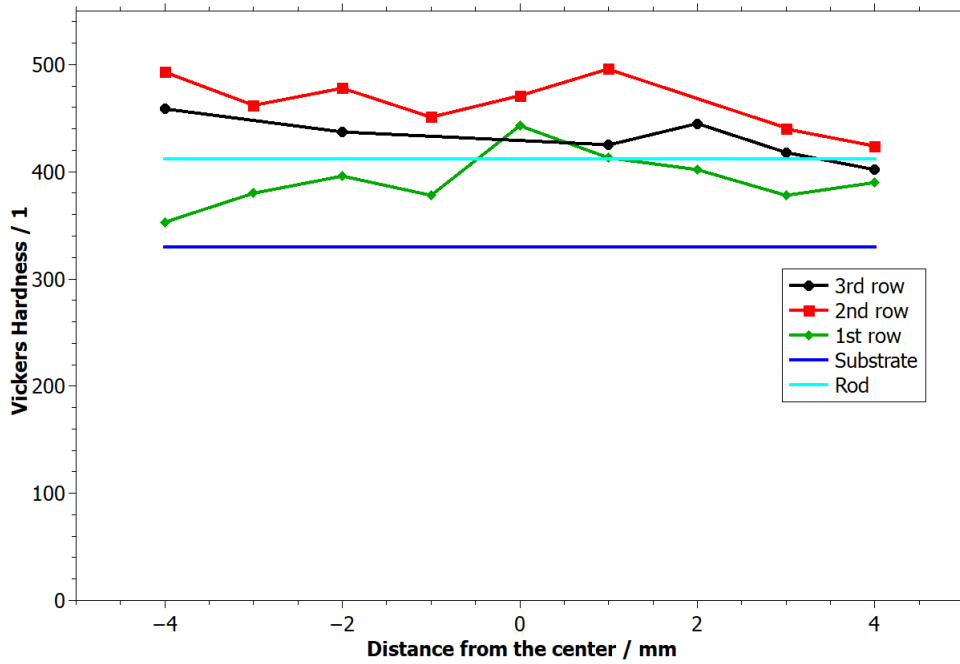


Fig. 5.29: Hardness in relation to the distance from the center for the double-layer.

The values show that the hardness of the first row behaves similarly to the raw material of the rod. By moving to the second row (which in terms of position would correspond to the top of the first layer, approximately), hardness increases possibly due to the presence of clusters of harder α -case regions that were not eliminated during the deposition of the second layer. The third row has hardness values only slightly greater than the ones found at the first row. Taking into account that no important trends could be seen horizontally, the average hardness values could be interpreted as being statistically equal. Therefore, the mean values of the individual hardness lines, with the standard deviation for the error bars, were calculated for the single- and double-layer depositions and are presented in Fig. 5.30.

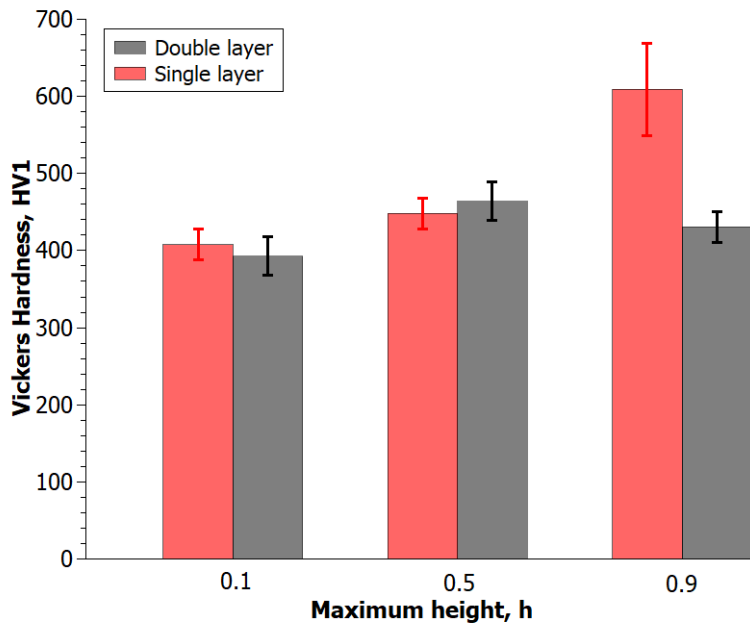


Fig. 5.30: Comparison of hardness of the single and double in relation to the maximum height of the layer.

In terms of hardness, stacking one layer to the other results in a deposition fundamentally different in comparison to a single-layer experiment. If considering the distances of the measurement lines with respect to the layer height h , it can be observed that at $0.9h$ single-layer depositions are much harder, since at those regions the presence of α -case already sets in. For double-layer depositions, the hardness is still fairly average at this particular point, which indicates that the hard α -case regions set in only beyond 90% of the layer, as it was observed in [16].

Moreover, the hardness at $0.5h$ of the double-layer deposition greatly differ from the measurements at $0.9h$ of the single-layer depositions. The comparison is relevant, since both positions represent virtually the same location in terms of absolute distance to the substrate, having theoretically both a large concentration of α -case regions and therefore similar hardness. Here, two explanations may be possible. The first considers that the first layer is slightly pushed down as the second one is deposited, which displaces the α -case clusters. Since the hardness measurements were done in a straight line, many points would miss the α -case layer, which would be no longer straight. The second possible explanation may be the dissolution of the α -case at the top of the first layer during the deposition of the second. While that may have happened to a certain extent, higher values of the second row in comparison to first and third ones (Fig. 5.30) may show that some harder regions may still have been present. Furthermore, the porosity observed at the interface of the two layers (Fig. 5.27) is surrounded by small α -grains, which may have been present before, indicating that an eventual dissolution of this phase would not have been complete. Further confirmation to those features is needed.

6 Summary and Outlook

In this work it was possible to use the Friction Surfacing to successfully deposit Ti-64 on Ti-64 substrates, using rods with smaller diameters than previously reported on the literature (8 mm and 12 mm).

The 8 mm experiments showed that such small diameters are not optimal for the FS process since the surface area does not provide enough heat generated by friction. On the other hand, layers deposited with 12 mm rods showed a more homogenous appearance, with the thickness increased to 1.3 mm at the center.

Furthermore, two consecutive layers with 12 mm could be deposited, without a machining step in-between. The irregular shape of the bottom layer decreased the contact surface, decreasing frictional heat generation and thus disrupting the shear layer formation during shortening stage. Hardness measurements data for the double-layer depositions showed that the values are similar to the single-layer ones.

Generally, the β -transus temperature is exceeded during the process and the cooling rate is high enough to form martensite, which is most abundant microstructural feature across the deposited layers. Occasional vortex shaped α -grain clusters could be also detected, which were normally associated to the presence of pores. Porosity was also observed elsewhere, especially at the retreating side. Furthermore, on double-layer depositions, the second layer showed a grain enlargement in comparison to the first one.

Further studies in this area would require an equipment with higher maximum displacement in the z-direction, in order to generate longer depositions. A specially designed sample holder would also provide a higher stability to the depositions, preventing wobbling and slippage. Moreover, to further close out the knowledge gap with respect to the influence of rod diameters on the FS of Ti-64, additional trials with diameters ranging between 13-19 mm could be done in the future. As for the double-layer experiments, the parameters for the shortening stage must be adapted accordingly taking into account the roughness of the underlying layer, considerably higher than the one from the substrate.

References

- [1] GANDRA, J. ; KROHN, H. ; MIRANDA, R.M ; VILAC, P. ; QUINTINO, L. ; DOS SANTOS, J.F.: Friction surfacing - A review. In: *Journal of Materials Processing Technology* (2013)
- [2] GANDRA, J. ; PEREIRA, D. ; MIRANDA, R.M. ; SILVA, R.J.C. ; VILAÇA, P.: Deposition of AA6082-T6 over AA2024-T3 by friction surfacing - Mechanical and wear characterization. In: *Surface and Coatings Technology* (2013)
- [3] VILAÇA, P. ; GANDRA, J. ; VIDAL, C.: *Linear Friction Based Processing Technologies for Aluminium Alloys: Surfacing, Stir Welding and Stir Channeling*. INTECH, 2013
- [4] BEDFORD, G.M. ; VITANOV, V.I. ; VOUTCHKOV, I.I.: On the thermo-mechanical events during friction surfacing of high speed steels. In: *Surface and Coatings Technology* (2001)
- [5] VILAC, P. ; GANDRA, J. ; VIDAL, C.: Linear friction based processing technologies for aluminium alloys: surfacing, stir welding and stir channeling. In: *Aluminium Alloys—New Trends in Fabrication and Applications* (2012)
- [6] NAKAMA, D. ; KATOH, K. ; TOKISUE, H.: Some characteristics of AZ31/AZ91 dissimilar magnesium alloy deposits by friction surfacing. In: *Materials Transactions* (2008)
- [7] VALE, N. ; FITSEVA, V. ; URTIGA FILHO, S.L. ; DOS SANTOS, J.F. ; HANKE, S.: Comparison of Friction Surfacing Process and Coating Characteristics of Ti-6Al-4V and Ti Grade 1. In: *The Minerals, Metals & Materials Society* (2019)
- [8] HANKE, S. ; FISCHER, A. ; BEYER, M. ; DOS SANTOS, J.: Cavitation erosion of NiAl-bronze layers generated by friction surfacing. In: *Wear* (2011)
- [9] VITANOV, V.I ; VOUTCHKOV, I.I.: Process parameters selection for friction surfacing applications using intelligent decision support. In: *Journal of Materials Processing Technology* (2005)
- [10] RAFI, H.K. ; RAM, G.D.J. ; PHANIKUMAR, G. ; RAO, K.P.: Friction surfaced tool steel (H13) coatings on low carbon steel: a study on the effects of process parameters on coating characteristics and integrity. In: *Surface and Coatings Technology 205* (2010)
- [11] TOKISUE, H. ; KATOH, K. ; ASAHINA, T. ; USIYAMA, T: Mechanical properties of 5052/2017 dissimilar aluminum alloys deposit by friction surfacing. In: *Materials Transactions 47* (2006)
- [12] RAFI, H.K. ; RAM, G.D.J. ; PHANIKUMAR, G. ; RAO, K.P: Friction surfacing of austenitic stainless steel on low carbon steel: studies on the effects of traverse speed. In: *World Congress on Engineering 2010* (2010)
- [13] SESHACHARYULU, T ; MEDEIROS, S.C. ; FRAZIER, W.G. ; PRASAD, Y.V.R.K.: Unstable flow during supratransus working of Ti-6Al-4V. In: *Materials Letters 47* (2001)
- [14] ARULSELVAN, M. ; GANESAN, G.: Hot deformation behaviour of Ti-6Al-4V in different strain rates. (2014)
- [15] SESHACHARYULU, T. ; MEDEIROS, S.C. ; FRAZIER, W.G. ; PRASAD, Y.V.R.K.: Hot working of commercial Ti-6Al-4V with an equiaxed alpha-beta microstructure: Materials modeling considerations. In: *Materials Science and Engineering A* (2000)
- [16] HANKE, S. ; STARON, P. ; FISCHER, T. ; FITSEVA, V. ; DOS SANTOS, J.F: A method for the in-situ study of solid-state joining techniques using synchrotron radiation - observation of phase transformations in Ti-6Al-4V after friction surfacing. In: *Surface & Coatings Technology* (2018)
- [17] BELEI, C. ; FITSEVA, V. ; DOS SANTOS, J.F. ; ALCÂNTARA, N.G. ; HANKE, S.: TiC particle reinforced Ti-6Al-4V friction surfacing coatings. In: *Surface & Coating Technology* (2017)
- [18] LOPES DO VALE, N. ; FITSEVA, V. ; HANKE, S. ; URTIGA FILHO, S.L. ; DOS SANTOS, J.F.: Influence of Rotational Speed in the Friction Surfacing of Titanium Grade 1 on Ti-6Al-4V. In: *Materials Research* (2017)
- [19] FITSEVA, V. ; HANKE, S. ; DOS SANTOS, J.F. ; STEMMER, P. ; GLEISING, B.: The role of process temperature and rotational speed in the microstructure evolution of Ti-6Al-4V friction surfacing coatings. In: *Materials and Design* (2016)

- [20] FITSEVA, V.: *Friction Surfacing of Titanium Grade 1 and Ti-6Al-4V*. Technische Universität Hamburg-Harburg, PhD Thesis, 2016
- [21] FITSEVA, V. ; KROHN, H. ; HANKE, S. ; DOS SANTOS, J.F.: Friction surfacing of Ti-6Al-4V: Process characteristics and deposition behaviour at various rotational speeds. In: *Surface & Coatings Technology* (2015)
- [22] GANDRA, J. ; VIGARINHO, P. ; PEREIRA, D. ; MIRANDA, R.M. ; VELHINHO, A. ; VILAÇ, P.: Wear characterization of functionally graded Al-SiC composite coatings produced by Friction Surfacing. In: *Materials & Design* (2013)
- [23] SHEN, J. ; HANKE, S. ; ROOS, A. ; DOS SANTOS, J.F. ; KLUSEMANN, B.: Fundamental Study on Additive Manufacturing of Aluminum Alloys by Friction Surfacing Layer Deposition. In: *AIP Conference Proceedings 2113*, 2019
- [24] MELD: *MELD Technology Solid-State Additive Manufacturing*. <http://meldmanufacturing.com/wp-content/uploads/2018/08/MELD-Overview.pdf>. Version: 29.9.2020
- [25] MELD: *Brochure*. <http://meldmanufacturing.com/>. Version: 29.9.2020
- [26] MELD: *How Does MELD Compare to FSAM?* <http://meldmanufacturing.com/wp-content/uploads/2018/05/How-Does-MELD-Compare-to-FSAM.pdf>. Version: 29.9.2020
- [27] LÜTJERING, G. ; WILLIAMS, J.: *Titanium*. Springer, 2007
- [28] LEYENS, C. ; PETERS, M.: *Titanium and Titanium alloys*. Wiley-VCH, 2003
- [29] AHMED, T. ; RACK, H.J.: Phase transformations during cooling in alpha+beta titanium alloys. In: *Materials Science and Engineering* (1998)
- [30] ASTM: *ASTM B265-20a: Standard Specification for Titanium and Titanium Alloy Strip, Sheet, and Plate*. West Conshohocken, 2020. <http://www.astm.org/cgi-bin/resolver.cgi?B265>
- [31] U.S. TITANIUM INDUSTRY, Inc.: Titanium Alloys - Ti-6Al-4V Grade 5. (2020). <https://www.azom.com/properties.aspx?ArticleID=1547>
- [32] BELEI, C.: *Evaluation of Ti-6Al-4V friction surfacing coatings reinforced with carbides*. Universidade federal de Sao Carlos, Master Thesis, 2017
- [33] ASTM: *ASTM E92-17: Standard Test Methods for Vickers Hardness and Knoop Hardness of Metallic Materials*. West Conshohocken, 2017. <http://www.astm.org/cgi-bin/resolver.cgi?E92>
- [34] TALYOR, B. ; WEIDMANN, E.: *Metallografische Präparation von Titan*. Struers, 01 2020. <https://www.struers.com/de-DE/Knowledge/Materials/Titanium>
- [35] GANDRA, J. ; MIRANDA, R.M. ; VILACA, P.: Performance analysis of friction surfacing. In: *Journal of processing technology* (2012)
- [36] KLIGERMAN, Y. ; VARENBERG, M.: Elimination of Stick-Slip Motion in Sliding of Split or Rough Surface. In: *Tribology letters* (2013)
- [37] XUE, Q. ; MEYERS, M.A. ; NESTERENKO, V.F.: Self-organization of shear bands in titanium and Ti-6Al-4V alloy. In: *Acta Materialia 50* (2001)
- [38] MOTYKA, M. ; KUBIAK, K. ; SIENIAWSKI, J. ; ZIAJA, W.: Hot Plasticity of Alpha-Beta-Alloys. (2012)
- [39] DEMTRÖDER, W.: *Experimentalphysik 1: Mechanik und Wärme*. Springer, 2017
- [40] MEHTA, M. ; ARORA, A. ; DE, A. ; BEBROY, T.: Tool Geometry for Friction Stir Welding-Optimum Shoulder Diameter. In: *Metallurgical and Materials Transactions A* (2011)

List of Figures

3.1	Stages of Friction Surfacing: (a) Rod is rotating with the rotational speed Ω ; (b) Axial force \vec{F} is applied in the z-direction; (c) Shear layer is formed by frictional heat, also called the shortening stage; (d) Traverse speed v is applied to deposit the layer. Also, the torque, axial displacement and axial force curves are shown (e), where a sharp increase in force, as well as torque, is visible at the first contact between rod and substrate, followed by a constant trend during the deposition. Adapted from [2].	8
3.2	(a) Cross section of layer with the rod; (b) Process variables; (c) Thermomechanical regions of FS, where the viscoplastic region forms between the deposition and the elastoplastic region [3].	9
3.3	Typical shape of FS layers for different aluminium alloys. a) AISI H13 over AISI 1020 [10]; b) AA2017 over AA5052 [11] and c) AISI 310 over AISI 1020 [12].	9
3.4	Depositions of Ti-64 with a 20 mm rod. (a) Layers with corresponding rotational speeds; (b) Micrographs of the respective layers [20].	10
3.5	Construction of an AA6082-T6 additive manufactured part of with the FS process: (a) multilayer deposition; (b) produced bulk; (c) height of deposition; (d) post machining [3].	11
3.6	Multi layer deposition of AA5083 on a AA2024 substrate produced with the FS process: (a) top view, (b) side view with the individual layers [23].	11
3.7	Types of structures successfully deposited by MELD [25].	12
3.8	Schematic of the tool used by MELD, with a hollow rotating tool that increases process efficiency by suppressing the flash formation [26].	12
3.9	Tridimensional phase diagram with the alloys classified by the wt. % of their alloying elements [28].	13
3.10	(a) Fully lamellar, (b) bi-modal and (c) fully equiaxed microstructure [27].	13
3.11	Difference in microstructure caused by the cooling rate for Ti-64. a), c), e) shows a pure lamellar microstructure, achieved with furnace cooling and in b), d), f) the martensite is formed with water quenching [28].	14
4.1	MTS Friction stir welding machine used in this work.	16
4.2	Process of establishing the parameter sets.	17
4.3	Quality features of the FS process (images are illustrative); (a) Absence of flash on the layer; (b) Homogeneity; (c) Straightness; (d) Thickness.	17
4.4	Schematics of the positioning of the thermocouple [32].	18
4.5	Position of the thermocamera in relation to the deposition.	18
4.6	Layer with indicated position of the cut for the cross sections.	19
5.1	Difference in appearance for depositions with different travel speeds, keeping other parameters constant: (a) 3000 min^{-1} , 0.2 kN, (b) 1500 min^{-1} , 0.5 kN.	20
5.2	Comparison of depositions with (a) deposition-rate (3000 min^{-1} , $42 \text{ mm}^3/\text{s}$) and (b) force-controlled mode (1400 min^{-1} , 0.5 kN).	21
5.3	Types of depositions with 8 mm rods and all with 500 mm/min traverse speed. (a) Type I: 1000 min^{-1} , 0.6 kN; (b) Type IIa: 1400 min^{-1} , 0.5 kN; (c) Type IIb: 1500 min^{-1} , 0.3 kN; (d) Type III: 2000 min^{-1} , 0.3 kN.	22
5.4	Different types of layers achieved with the 8 mm rod and their corresponding rotational speed, axial force with a constant traverse speed of 500 mm/min. Type I (blue), Type IIa (dark green), Type IIb (green) and Type III (red) are listed.	23
5.5	Micrograph of a cross section of the 8 mm deposition with 1400 min^{-1} and 0.5 kN.	24
5.6	SEM images of the cross section of a deposition with an 8 mm rod (1400 min^{-1} , 0.5 kN).	24
5.7	Map of microstructural changes occurring during hot processing of Ti-64. Black triangle estimates the position of the FS as a process relative to the diagram. Adapted from [38].	25
5.8	Position of the hardness line on an 8 mm rod deposition.	25
5.9	Hardness values for the 8 mm rod deposition in relation to the distance from the center.	26
5.10	Impact of insufficient energy input during the shortening stage on the layer quality; 0.7 kN shortening force and 1.0 mm displacement.	27

5.11 (a) Deposition with a 12 mm rod and (b) corresponding flash; 3000 min ⁻¹ , 0.5 kN, 800 mm/min.	27
5.12 Micrograph of a deposition with 3200 min ⁻¹ and 0.8 kN. In comparison to the 8 mm deposition the thickness is increased to 1.3 mm at the center. The layer shows unbonded edges on the RS but not on the AS.	28
5.13 Different types of layers achieved with the 12 mm rod and their corresponding rotational speed, axial force, and a constant traverse speed of 700 mm/min. The areas for Type I (blue) and Type II (green) can be seen.	28
5.14 Impact of the force on the visual appearance of a 12 mm deposition. Force is varied from 0.5 to 1 kN, while rotational speed and travel speed are kept constant.	29
5.15 Change of Energy Input per volume for different axial forces.	30
5.16 Position of the thermocouple in the cross section. It is visible that the thermocouple is welded with the layer.	31
5.17 Temperature curve achieved by the thermocouple experiment, with the indicated maximum and β -transus temperature.	31
5.18 Thermocamera measurement at a distance of 1 meter and with an emissivity factor of 0.89.	32
5.19 Position of the measuring lines for the 12 mm single-layer deposition.	32
5.20 Hardness values of the single-layer in relation to the distance from the center.	33
5.21 Best possible depositions for 8 mm (a) 1400 min ⁻¹ , 0.5 kN and 500 mm/min); (b) 12 mm, 3000 min ⁻¹ , 0.5 kN and 800 mm/min); (c) 20 mm (adapted from [20]), 3000 min ⁻¹ , 2 kN and 960 min ⁻¹ rods.	33
5.22 Specific energy and torque in relation to the rod diameter.	34
5.23 Illustrative presentation of the model explaining the relation between torque and rod diameter.	35
5.24 Example of a double-layer achieved with a 12 mm rod (2 nd layer in the white dotted line). 1 st layer: 3200 min ⁻¹ , 0.5 kN, 700 mm/min; 2 nd layer: same as 1 st layer but displacement of the shortening stage was altered to 1.5 mm.	35
5.25 Micrograph of a cross section of the 12 mm rod double-layer deposition.	36
5.26 (a) Micrograph of the double-layer with detailed images from the (b) first and (c) second layer.	36
5.27 Micrograph (a) with SEM images from retreating side (b) showing the martensitic matrix and advancing side (c) with pores (visible as dark spots) and the presence of α -grains.	37
5.28 Position of the hardness lines for the double-layer deposition.	37
5.29 Hardness in relation to the distance from the center for the double-layer.	38
5.30 Comparison of hardness of the single and double in relation to the maximum height of the layer.	38

List of Tables

4.1	Alloying elements of Ti-64 according to ASTM B265-20a [30].	15
4.2	Dimension and material of the used substrate and rods.	15
4.3	Material properties of Ti-64 [31].	15
4.4	Specifications of the Friction Stir Welding machine.	15
4.5	Polishing steps used for the metallographic procedure [34].	19
4.6	Solution used for the etching of the cross sections (Kroll's reagent).	19
5.1	Parameter window for the 8mm experiments.	20
5.2	Parameter ranges for the achieved deposition types.	23
5.3	Parameter window for the 12 mm rod experiments.	26
5.4	Parameter ranges for the achieved deposition types with 12 mm rods.	28